





Enhancing 4-D Landslide Monitoring and Block Interaction Analysis With a Novel Kalman-Filter-Based InSAR Approach

Wanji Zheng^{1,2,3} , Jun Hu¹ , Zhong Lu² , Xie Hu⁴ , Qian Sun⁵ , Jihong Liu¹ , and Bo Huang³ 

¹School of Geosciences and Info-Physics, Central South University, Changsha, China, ²Roy M. Huffington Department of Earth Sciences, Southern Methodist University, Dallas, TX, USA, ³Department of Geography, The University of Hong Kong, Hong Kong, China, ⁴College of Urban and Environmental Sciences, Peking University, Beijing, China, ⁵College of Resources and Environmental Science, Hunan Normal University, Changsha, China

Key Points:

- A novel method is proposed for estimating 4-D landslide movements using spaceborne synthetic aperture radar interferometric observations
- 4-D movements of the Hooskanaden landslide are derived to infer landslide's strain invariants, block count, and slip surface distribution
- Prior to the catastrophic event in February 2019, an anomalous strain invariant signal of the Hooskanaden landslide was detected

Supporting Information:

Supporting Information may be found in the online version of this article.

Correspondence to:

J. Hu,
csuhujun@csu.edu.cn

Citation:

Zheng, W., Hu, J., Lu, Z., Hu, X., Sun, Q., Liu, J., & Huang, B. (2024). Enhancing 4-D landslide monitoring and block interaction analysis with a Novel Kalman-filter-based InSAR approach. *Journal of Geophysical Research: Earth Surface*, 129, e2024JF007923. <https://doi.org/10.1029/2024JF007923>

Received 7 JUL 2024

Accepted 11 OCT 2024

Author Contributions:

Conceptualization: Wanji Zheng, Jun Hu
Data curation: Zhong Lu

Formal analysis: Wanji Zheng, Qian Sun, Jihong Liu

Funding acquisition: Jun Hu, Bo Huang

Investigation: Wanji Zheng, Xie Hu, Qian Sun

Methodology: Wanji Zheng, Jun Hu, Jihong Liu

Project administration: Jun Hu, Bo Huang

Resources: Jun Hu, Zhong Lu

Software: Zhong Lu

Supervision: Jun Hu, Zhong Lu

Validation: Wanji Zheng, Xie Hu, Jihong Liu

Visualization: Wanji Zheng, Xie Hu

Writing – original draft: Wanji Zheng, Jun Hu, Zhong Lu, Xie Hu

Writing – review & editing:

Wanji Zheng, Jun Hu, Zhong Lu, Xie Hu

Abstract In recent years, Synthetic Aperture Radar Interferometry (InSAR) has become widely utilized for slow-moving landslide monitoring due to its high resolution, accuracy, and extensive coverage. By integrating data from various orbits/platforms and monitoring sources, one-dimensional (1-D) line-of-sight (LOS) InSAR measurements can be explored to infer three-dimensional (3-D) movements. However, inconsistencies in observation times among different orbits and monitoring sources pose challenges in accurately capturing dynamic 3-D movements over time (referred to as 4-D). In this study, we propose a novel method, termed KFI-4D that incorporates spatiotemporal constraints into the traditional Kalman filter. This enhancement transforms the underdetermined problem of 4-D movement acquisition into a dynamic parameter estimation problem, enabling precise monitoring of landslide movements. The KFI-4D method was evaluated using both synthetic data sets and real data from the Hooskanaden landslide, demonstrating an improvement exceeding 50% in root mean square errors (RMSEs) compared to conventional methods. Additionally, the high-resolution characteristics of InSAR-derived 4-D movements allow for the analysis of strain invariants, providing insights into block interactions and landslide dynamics. Our findings reveal that strain invariants effectively indicate the distribution and activity of landslide blocks and slip surfaces as well as their response to triggers. Notably, abnormal signals identified in strain invariants prior to the catastrophic event at Hooskanaden suggest potential for early warning of landslides. The future integration of data from advanced satellites, such as NISAR, ALOS4 PALSAR3, and Sentinel-1C, is expected to further enhance the KFI-4D method's capabilities, improving temporal resolution and early warning potential for landslide monitoring.

Plain Language Summary InSAR, a radar technology, is a powerful tool for monitoring landslides, providing detailed and accurate displacement data. Combining data from multiple sources offers a more complete picture of 3-D displacements. However, satellites observe at different times, making it challenging to get an accurate picture of slow-moving landslide movements over time (4-D monitoring). To address this, we developed KFI-4D, a new method that enhances the traditional Kalman filter by adding space and time constraints and improving the tracking of landslide movements in 4-D. Testing with both simulated data and real data from the Hooskanaden landslide showed that KFI-4D improved accuracy by over 50% compared to the traditional method. Our method also helps to study how different parts of a landslide interact. We found that analyzing these interactions can provide important insights into the behavior and triggers of landslides. Notably, unusual signals detected before the major event of the Hooskanaden landslide suggest that our method could be useful for early warning systems. Overall, KFI-4D could make landslide monitoring more accurate and reliable, allowing for more data from different satellites and enhancing the monitoring process. Future satellites are expected to further improve this method, making it even more effective for early warning of landslides.

1. Introduction

Under the influence of multiple driving factors, slow-moving landslides can experience a reduction in shear strength and/or an increase in shear stress, which subsequently diminishes the stability of the landslide, leading to accelerated movement or even collapse (Lacroix et al., 2020). The simultaneous impact of multiple factors adds complexity to the study of slow-moving landslide mechanisms. In recent decades, the advancement of spaceborne Interferometric Synthetic Aperture Radar (InSAR) technology has provided a comprehensive and innovative

approach for geohazard research (Karanam & Lu, 2023; Y. Xu, Schulz, et al., 2021). Based on the high spatial resolution capabilities of InSAR observations, varying responses to triggering factors can be observed in different sections of a landslide (X. Hu, Bürgmann, et al., 2019). Through the utilization of spaceborne InSAR's long-term global monitoring capabilities, unknown landslides can be retrospectively studied using archived data, enabling an understanding of their past dynamics and the implementation of targeted disaster management strategies (A. L. Handwerger et al., 2019; X. Liu et al., 2020). However, current SAR satellites are predominantly polar-orbiting and employ right-looking observations. As a result, spaceborne InSAR can only capture the projected deformation of landslides along the line of sight (LOS), limiting its application in landslide studies (J. Hu et al., 2014).

To address the challenge of deriving three-dimensional (3-D) movements of slow-moving landslides using spaceborne InSAR, researchers have developed a series of new techniques over the past two decades. These techniques encompass the integration of multiple independent InSAR measurements (Alexander L. Handwerger et al., 2021; X. Hu et al., 2020), azimuth deformation-assisted methods (Shi et al., 2021; C. Wang et al., 2018), and model-constrained methods (J. Hu et al., 2017; Zheng et al., 2023). By combining multi-temporal and multi-source SAR data, it is possible to further obtain the four-dimensional (4-D) deformation of slow-moving landslides (three dimensions in space plus one dimension in time domain, also known as dynamic 3-D deformation). The acquisition of 4-D deformation using InSAR technology offers a unique and invaluable perspective for landslide studies, enabling the estimation of landslide thickness and facilitating the quantification of landslide rheology (X. Hu et al., 2020). However, obtaining 4-D deformation of landslides requires the multi-temporal and multi-source observations, with different observations having different acquisition times. Consequently, acquiring 4-D deformation using spaceborne InSAR technology becomes an underdetermined problem (Samsonov, 2019), limiting the potential of InSAR technology in capturing 4-D deformation.

Currently, there is limited research on the acquisition of 4-D deformation of slow-moving landslides using InSAR technology. X. Hu et al. (2020) successfully obtained the 4-D deformation of the Slumgullion landslide using airborne SAR data. In this particular case, the temporal differences between observations from different orbits were relatively small, allowing for the temporal variations to be disregarded, thus facilitating the acquisition of 4-D deformation. However, achieving similar results in most areas where only spaceborne SAR data are available poses significant challenges. To address the underdetermined problem of obtaining 4-D deformation of landslides, Samsonov et al. (2020) proposed a novel version of the Multidimensional Small Baseline Subset (MSBAS-3D) technique. This technique, based on the principles of Tikhonov regularization, utilizes the L-curve method to determine the regularization parameter and employs it as a constraint for estimating 4-D deformation. However, it is worth noting that this method exhibits reduced robustness in the presence of substantial observation noise (J. Liu, Hu, Li, Sun, et al., 2022). In landslide scenarios where decorrelation noise and atmospheric noise significantly affect the data, acquiring reliable 4-D deformation using this approach becomes challenging.

Kalman filter is a dynamic estimation technique that can transform the underdetermined problem encountered in the fusion of multi-source SAR data sets into a dynamic estimation problem (Dalaison & Jolivet, 2020; J. Hu et al., 2013). Currently, it has found applications in the integration of InSAR and GPS (N. Liu et al., 2018) as well as in the field of two-dimensional deformation retrieval using spaceborne InSAR (J. Liu, Hu, Li, Sun, et al., 2022). The key to the Kalman filter lies in constructing the state transition equation and the state update equation. To address the impact of multiple noise sources in InSAR landslide monitoring and achieve more robust 4-D movement measurements, this study introduces a spatiotemporally constrained Kalman filter-based InSAR method for deriving 4-D landslide movements, referred to as KFI-4D. This method incorporates spatiotemporal constraints in the state transition equation and the state update equation, and introduces a Huber's weighting function (Yang et al., 2002) in the state update equation.

The performance of the proposed method is validated using both synthetic and real data sets, specifically the Hooskanaden landslide on the West Coast of the United States. The West Coast is known to be severely affected by geological disasters, particularly catastrophic landslides caused by heavy rainfall during storms. These events not only result in damage to local buildings but also pose a serious threat to drivers on CA #1 and US #101. Despite the significance of these events, the application of InSAR technology in studying the 4-D movement of landslides on the West Coast is relatively uncommon due to variations in imaging time and observation errors among SAR satellites in multiple platforms/tracks. The Hooskanaden Landslide, one of the largest landslides on the West Coast, experienced a catastrophic event in February 2019 following heavy rainfall. In this study, we utilized the proposed KFI-4D method and data from Sentinel-1A/B ascending and descending tracks to estimate

the 4-D movements of the Hooskanaden Landslide from July 2016 to February 2019. It is important to note that landslide movement often involves the interaction of multiple blocks rather than a single mass moving independently. To understand these interactions, strain invariants play a critical role. This work not only calculates strain invariants using the high spatial resolution characteristics of InSAR but also explores the dynamics of strain invariants by analyzing the 4-D movements of the Hooskanaden Landslide. Analyzing the variations of these strain invariants will help reveal the dynamic interactions among different blocks of the Hooskanaden landslide, providing a new perspective to gain deeper insights into the progressive development of the Hooskanaden landslide under the influence of triggering factors, ultimately leading to the catastrophic event in 2019.

2. Study Area and Data Sets

The West Coast region, encompassing California, Oregon, and Washington, has long been recognized as one of the most susceptible areas to landslides in the United States due to factors such as tectonic movements, weak lithologies, and heavy rainfall associated with storms (Alberti et al., 2020). In order to address this issue, landslide detection efforts have been conducted in this coastal area utilizing InSAR technology. The findings revealed a total of 617 active landslides, out of which 588 were previously unrecorded (Y. Xu, Schulz, et al., 2021). Furthermore, previous research has indicated that the type of bedrock in the region plays a crucial role in determining the size and density distribution of landslides, while rainfall exerts a strong influence on the spatial distribution pattern of these occurrences (Y. K. Xu, George, et al., 2021). It is important to note that along the Pacific coast, where landslides are widespread, there is a population of 32 million individuals. During storm events, the frequent incidence of landslide disasters often results in road closures, isolating certain areas and inflicting significant economic and social consequences.

The Hooskanaden landslide is situated in Curry County, Oregon, on the west coast of the United States, approximately 25 km from the northern border of California. US Highway 101 traverses through the landslide (Figure 1a). The landslide extends over a length of more than 1 km, with a maximum width of 550 m and a total coverage area of 405,000 m². The estimated volume of the landslide is approximately $1.4\text{--}2.1 \times 10^6$ m³. The earthflow is characterized by intensely sheared rocks and heterogeneous mixtures of serpentinite blocks (Parker, 1979). The primary lithological components of the landslide comprise sandstone, siltstone, and mudstone. Notably, the landslide material is highly fragmented, exhibiting minimal residual bedding (Alberti et al., 2020). Over the past few decades, the landslide has experienced several significant events, particularly in 1977, followed by two more destructive failures in 1995 and 2019, with approximately 20 years's separation in between (Alberti et al., 2020).

High-resolution LiDAR data revealed significant past movements and surface marks of the landslide (dashed green lines in Figure 1a). Figure 1b demonstrates long-term slow creep motion scratches on the landslide surface, accompanied by tensile cracks and notable scarps at the rear edge, while Figure 1c shows the optical image for comparison. The February 2019 event caused substantial road damage (Figures 1d and 1e). Analyses using LiDAR data from multiple periods revealed a vertical displacement of 12 m and a horizontal movement of 45 m (Alberti et al., 2020). The event resulted in a two-week closure of US Highway 101, causing an economic loss of about 3.7 million dollars. It was reported that this significant event could be attributed to dense winter rainfall in 2019 based on the time-series analysis using Sentinel-1 data (Xu et al., 2020). However, it was evident that the strength of total rainfall alone could not accurately describe the occurrence of major landslide events (Alberti et al., 2020). Field geological surveys, complemented by limited subsurface observation data, revealed that the landslide comprises several distinct blocks rather than being controlled by a single sliding surface (Parker, 1979). Individual blocks move along the failure surfaces determined by lithology and planes of weakness (Alberti et al., 2020). Hence, our study aimed to utilize high-resolution InSAR 4-D measurements to investigate the interaction dynamics between these blocks, which could yield a comprehensive understanding of the failure mechanism, offering novel insights for subsequent landslide monitoring and early warning strategies.

In order to analyze the 4-D movements of the Hooskanaden landslide using InSAR technology, we obtained two tracks consisting of over 110 scenes of Sentinel-1A/B data from July 2016 to February 2019 (i.e., the T13 and T35 tracks shown in the bottom right subplot of Figure 1a). It is noteworthy that an additional distinct third track of Sentinel-1 data sets is available (depicted as the S1-T108 track in the subplot of Figure 1a). This track presents an opportunity to independently validate the proposed method and was one of the reasons why this area was chosen as the test site. Additionally, we obtained the Copernicus Global DEM to eliminate the topographic phase in the

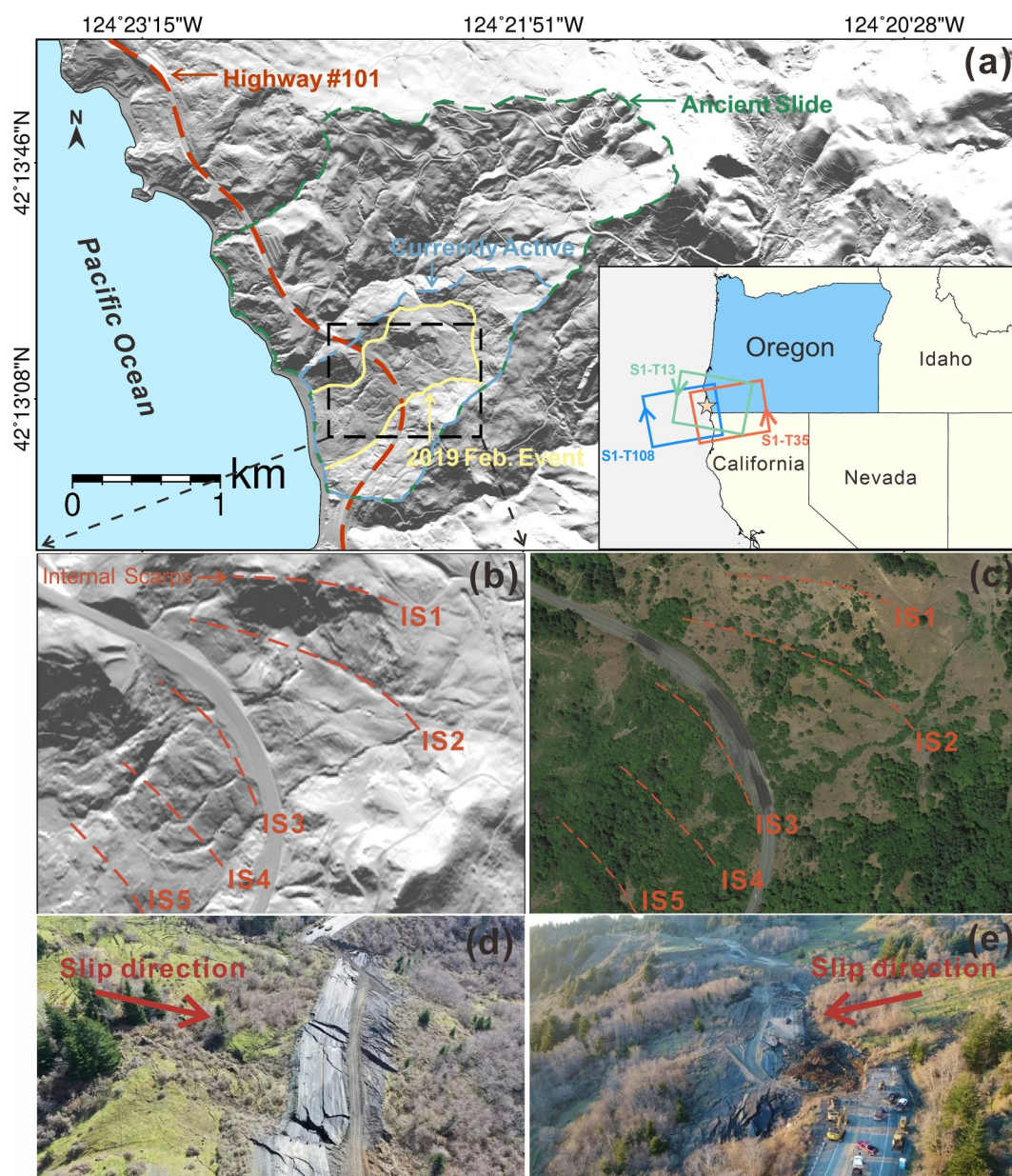


Figure 1. Overview of the Hooskanaden landslide. (a) A shaded relief map generated from a LiDAR DEM, along with the geographical location of the landslide marked by a pink star in the bottom right corner. (b) Detailed shaded relief map of the landslide, featuring internal scarps (IS) delineated based on the progress report by Parker (1979). (c) A Google Earth image capturing the landslide area. (d and e) Photographs depicting the February 2019 slide event (Xu et al., 2020).

InSAR processing chain. More detailed information about the utilized SAR data sets are summarized in the Table S1 of Supporting Information S1.

3. Methodology

The Kalman filter plays a crucial role in the processing of multi-source data fusion (Dalaison & Jolivet, 2020; J. Hu et al., 2013; N. Liu et al., 2018). It employs a series of mathematical models to describe dynamic systems, particularly the state transition equation (STE) and the state update equation (SUE). The STE utilizes a specific motion model that leverages historical data, including the state vector and its variance-covariance matrix, to predict the future state of the system. Subsequently, when the observation system acquires observations for the

next epoch, it updates the current state by combining the predicted system state with the SUE. This iterative process enables the dynamic estimation of the system state. In general, this process can be succinctly represented by a common Kalman filter formula:

$$\begin{cases} \hat{X}_i^- = F \hat{X}_{i-1} \\ D_{\hat{X},i}^- = F D_{\hat{X},i-1} F^T + Q_i \\ K_k = D_{\hat{X},i}^- H^T (H D_{\hat{X},i-1} H^T + D_L)^{-1} \\ \hat{X}_i = \hat{X}_i^- + K_k (L - H \hat{X}_i^-) \\ D_{\hat{X},i} = (E - K_k H) D_{\hat{X},i}^- \end{cases} \quad (1)$$

where \hat{X}_i^- and \hat{X}_i represent the predicted and estimated 3-D displacements of the state vector at i^{th} time, respectively, with the hat symbol indicating that the variable represents an estimate. Our aim is to obtain the 4-D movements of landslides, and similar to conventional temporal InSAR approaches, we assume the deformation at time zero to be zero, such that the state vector at the i^{th} time step represents the cumulative 3-D displacements. To link the state vectors at i^{th} time and $(i-1)^{\text{th}}$ time, the Kalman filter typically requires the design of a state transition matrix F in the state transition equation $\hat{X}_i^- = F \hat{X}_{i-1}$, based on the motion of the dynamic system, to perform dynamic prediction of the state vectors. Furthermore, to suppress the noise in the Kalman filter system, the dynamic update of the state vector in the SUE $\hat{X}_i = \hat{X}_i^- + K_k (L - H \hat{X}_i^-)$ requires a variance-covariance matrix that considers the noise corresponding to the state and observation at different times. In Equation 1, $D_{\hat{X},i}^-$, $D_{\hat{X},i}$, and D_L are the variance-covariance matrix of the predicted state vector \hat{X}_i^- , the estimated state vector \hat{X}_i , and the observation vector L , respectively. Q_i represents the state transition variance-covariance matrix, which accounts for the inevitable discrepancies between the actual deformation and the forecast (Dalaison & Jolivet, 2020). The gain matrix K_k in the SUE plays a vital role in updating the state vector and can be constructed using the projection vector H , the variance-covariance matrix of the observation value D_L , and the variance-covariance matrices of the predicted state vector $D_{\hat{X},i}^-$ and the estimated state vector $D_{\hat{X},i}$.

The performance of the Kalman filter implementation greatly relies on the establishment of the STE and the SUE based on the dynamic system conditions. In light of this, the method proposed in this study aims to leverage the spatiotemporal characteristics of landslide motion to constrain the STE and SUE of the Kalman filter, thereby achieving robust estimation of the 4-D movements from InSAR observations. In the following sections, we will delve into the details of the spatiotemporally constrained STE and spatially constrained SUE within the KFI-4D method. Additionally, we will provide an overview of the data processing procedures employed in this work, followed by an implementation instruction for the KFI-4D method.

3.1. Spatiotemporally Constrained State Transition Equation

The state transition equation (STE) serves as a crucial tool for predicting the state vector within the Kalman filter framework. In KFI-4D, this equation facilitates the prediction of 3-D landslide movements in subsequent epochs. Conventionally, InSAR time-series processing methods utilizing the Kalman filter have only accounted for the relationship between time $i-1$ and i in STE, without accounting for the relationship between 3-D deformations (J. Hu et al., 2013; J. Liu, Hu, Li, Sun, et al., 2022). However, these methods face limitations due to their insensitivity to north-south deformation in InSAR results, hindering the acquisition of 3-D movements for a given epoch. Consequently, these methods often yield only dynamic 2-D deformations, disregarding the north-south deformation component. To overcome this limitation and accurately obtain 3-D landslide movements, several studies have demonstrated the efficacy of incorporating surface parallel flow (SPF) as a constraint on the 3-D movements of landslides (Joughin et al., 1998; Samsonov et al., 2020; Zheng et al., 2023). This approach enhances the precision of landslide 3-D movement using InSAR technology. Thus, in the STE of KFI-4D, we integrate SPF as a spatial constraint. As a result, the predicted state vector value $\hat{x}_i^- = [\hat{x}_{e,i}^- \ \hat{x}_{n,i}^- \ \hat{x}_{v,i}^-]^T$ at time i can be expressed through the subsequent equation:

$$\hat{x}_i^- = \begin{bmatrix} F_e & F_n & F_v \end{bmatrix}^T \begin{bmatrix} \hat{x}_{e,i-1} & \hat{x}_{n,i-1} & \hat{x}_{v,i-1} \end{bmatrix}^T \quad (2)$$

where F_e , F_n , and F_v represent the state transition vectors corresponding to the 3-D deformations $\hat{x}_{e,i-1}$, $\hat{x}_{n,i-1}$, and $\hat{x}_{v,i-1}$, respectively. By incorporating the slope constraint (i.e., the ratio of vertical to horizontal movement equals the slope gradient) and the aspect constraint (i.e., horizontal movement aligns with the aspect direction) of the SPF, this part can be expressed as:

$$F = \begin{bmatrix} F_e \\ F_n \\ F_v \end{bmatrix} = \begin{bmatrix} 1 & 0 & 0 \\ \cos(\theta_{asp}) \cdot \sin(\theta_{asp}) & 0 & 0 \\ \theta_e & \theta_n & 0 \end{bmatrix} \quad (3)$$

where θ_{asp} represents the slope aspect on the corresponding pixel of InSAR observation measured in radians, while θ_e and θ_n denote the eastward and northward components of the slope gradient at the pixel, both dimensionless. Therefore, Equation 2 incorporates terrain information to provide a constraint on the 3-D deformation, addressing the issue of InSAR's insensitivity to north-south deformation. However, it is important to note that Equation 2 only constraints the 3-D deformation between time i and time $i - 1$, without explicitly establishing a connection in the time domain to predict the deformation at time i based on observations at time $i - 1$. In previous InSAR techniques that use the Kalman filter, a linear model is commonly employed by incorporating the time interval between adjacent imaging moments as a parameter in matrix F (J. Hu et al., 2013; N. Liu et al., 2018). This enables prediction from the previous epoch to the next. However, landslide movement is often influenced by multiple factors such as rainfall and groundwater levels, exhibiting significant seasonal and fluctuating patterns. Linear deformation models alone are insufficient to effectively capture the complex movement of landslides. Furthermore, InSAR observations are susceptible to significant random noise and atmospheric interference, which reduces the reliability of 4-D deformation results. To address these limitations, the proposed method introduces a time-dependent smooth process constraint as a temporal constraint in the STE to connect observations from adjacent epochs and suppress the influence of noise (J. L. Wang et al., 2019). This constraint takes into account the correlation between observations at neighboring epochs, making it particularly suitable for slow-moving landslides. For instance, considering the eastward deformation $\hat{X}_{e,i-1}$ as an example, assuming the estimated deformations at time $i - 1$ and the previous n epochs in the eastward direction are $\hat{X}_{e,i-1} = [de_{i-1}, de_{i-2}, \dots, de_{i-n}]^T$, the following relationship holds between the deformations within these n epochs:

$$\hat{X}_{e,i-1} = B_i A_i = \begin{bmatrix} 1 & \Delta t_{i-1} & \Delta t_{i-1}^2 & \dots & \Delta t_{i-1}^m \\ 1 & \Delta t_{i-2} & \Delta t_{i-2}^2 & \dots & \Delta t_{i-2}^m \\ 1 & \vdots & \vdots & \ddots & \vdots \\ 1 & \Delta t_{i-n} & \Delta t_{i-n}^2 & \dots & \Delta t_{i-n}^m \end{bmatrix} \begin{bmatrix} \alpha_0 \\ \alpha_1 \\ \vdots \\ \alpha_m \end{bmatrix} \quad (4)$$

where Δt_{i-n} represents the time interval between the image at time $i - 1$ and the n^{th} preceding image, and m is the order of the polynomial used for fitting. The idea behind this constraint is that historical deformation is assumed to be fitted by time-dependent m -order polynomials, where $\alpha_0 - \alpha_m$ represents the polynomial coefficients. Then, the displacement at the current epoch can be predicted by this polynomial. In this study, we use $m = 3$. It should be noted that the n is an arbitrary constant. This allows for the prediction at time i , where the corresponding polynomial coefficients A_i can be estimated based on the polynomial coefficients A_{i-1} at time $i - 1$:

$$\hat{A}_i = Q_{\hat{A},i} Q_{\hat{A},i-1}^{-1} A_{i-1} + Q_{\hat{A},i} B_i^T \hat{X}_{e,i-1} \quad (5)$$

In the above Equation, $Q_{\hat{A},i}$ and $Q_{\hat{A},i-1}$ represent the variance-covariance matrices of A_i and A_{i-1} , respectively. These matrices can be calculated using B_i , which is constructed from the time interval and its higher-order powers (J. L. Wang et al., 2019):

$$Q_{\hat{A},i} = (B_i^T B_i)^{-1} \quad (6)$$

Let $\varepsilon_0 = Q_{\hat{A},i} Q_{A,i-1}^{-1} A_{i-1}$. By incorporating this into Equation 4, the eastward deformation $\hat{d}_{e,i}$ at time i can be calculated using the following equation:

$$\begin{aligned} \hat{d}_{e,i} &= [1 \quad \Delta t_i \quad \Delta t_i^2 \quad \cdots \quad \Delta t_i^m] \hat{A}_i + \varepsilon_0 \\ &= [1 \quad \Delta t_i \quad \Delta t_i^2 \quad \cdots \quad \Delta t_i^m] (B_i^T \cdot B_i)^{-1} B_i^T \hat{X}_{e,i-1} + \varepsilon_0 \end{aligned} \quad (7)$$

By introducing a vector that incorporates the intermediate variable β to represent the coefficients of $\hat{X}_{e,i-1}$ in Equation 7, we obtain:

$$[1 \quad \Delta t_i \quad \Delta t_i^2 \quad \cdots \quad \Delta t_i^m] (B_i^T \cdot B_i)^{-1} B_i^T = [\beta_{e,i-1} \quad \beta_{e,i-2} \quad \cdots \quad \beta_{e,i-n}] \quad (8)$$

Through the integration of the aforementioned derivation process, there exists the following relationship between $\hat{X}_{e,i}$ and $\hat{X}_{e,i-1}$:

$$\begin{aligned} \hat{X}_{e,i} &= B_e \hat{X}_{e,i-1} + E_0 \\ &= \begin{bmatrix} \beta_{e,i-1} & \beta_{e,i-2} & \beta_{e,i-3} & \cdots & \beta_{e,i-n} \\ 1 & 0 & 0 & \cdots & 0 \\ 0 & 1 & 0 & \cdots & 0 \\ \vdots & \vdots & \vdots & \ddots & \vdots \\ 0 & 0 & 0 & 1 & 0 \end{bmatrix} \begin{bmatrix} de_{i-1} \\ de_{i-2} \\ de_{i-3} \\ \vdots \\ de_{i-n} \end{bmatrix} + \begin{bmatrix} \varepsilon_0 \\ 0 \\ 0 \\ 0 \\ 0 \end{bmatrix} \end{aligned} \quad (9)$$

where B_e is a coefficient matrix constructed from β_e . Note that although we begin with Equation 4, where the displacement time series is modeled by time-dependent polynomials, the STE is only relevant to the epoch time (i.e., $\Delta t_i - \Delta t_{i-n}$) of the displacement time series after the derivation of Equations 4–7, and the polynomial coefficients (i.e., $\alpha_0 - \alpha_m$) in Equation 4 do not need to be estimated.

Hence, employing the aforementioned equations enables the prediction of the state vector at time i by incorporating constraints from the preceding n state vectors at earlier instances $i - 1, i - 2, \dots, i - n$. Similarly, for the deformation components aligned in the northward and vertical directions within the state vector, temporal constraints can be established as well. Presuming that the temporal constraint coefficients in the northward and vertical directions are denoted by B_n and B_v , respectively, and amalgamating Equations 2, 3 and 9, the state transition matrix representing the spatiotemporal constraints in the Kalman filter can be expressed as:

$$\hat{X}_i^- = \text{diag}(B_e \quad B_n \quad B_u) [F_e \quad F_n \quad F_u]^T [\hat{X}_{e,i-1} \quad \hat{X}_{n,i-1} \quad \hat{X}_{v,i-1}]^T \quad (10)$$

3.2. Spatially Constrained State Update Equation

The SUE of the Kalman Filter employs the system observation value L and the Kalman Filter gain matrix K_κ at time i to update the predicted state vector \hat{X}_i^- and achieve the objective of accurately estimating the state vector \hat{X}_i at time i by the following equation:

$$\hat{X}_i = \hat{X}_i^- + K_\kappa (L - H \hat{X}_i^-) \quad (11)$$

In previous studies, InSAR with Kalman filter often utilized the projection vector H , which is derived from SAR satellite imaging geometry, to connect the system observation value L with the predicted state vector \hat{X}_i^- (J. Hu et al., 2013; J. Liu, Hu, Li, Sun, et al., 2022). However, InSAR observations do not possess sensitivity toward the North-South deformation component. Consequently, relying solely on the projection vector H fails to provide an effective estimation of the North-South deformation component. To overcome this limitation, we propose the

introduction of SPF as a spatial constraint in the SUE, which enhances the estimation accuracy of the North-South deformation component:

$$\begin{aligned}
 L &= H[\hat{d}_{e,i}^- \quad \hat{d}_{n,i}^- \quad \hat{d}_{v,i}^-]^T = [h_e \quad h_n \quad h_v][\hat{d}_{e,i}^- \quad \hat{d}_{n,i}^- \quad \hat{d}_{v,i}^-]^T \\
 &= \begin{bmatrix} -\cos(\alpha_{az} - 3\pi/2) \sin(\alpha_{inc}) & -\sin(\alpha_{az} - 3\pi/2) \sin(\alpha_{inc}) & \cos(\alpha_{inc}) \\ \cos(\theta_{asp}) \cdot \sin(\theta_{asp}) & -1 & 0 \\ \theta_e & \theta_n & -1 \end{bmatrix} \begin{bmatrix} \hat{d}_{e,i}^- \\ \hat{d}_{n,i}^- \\ \hat{d}_{v,i}^- \end{bmatrix} \\
 &= [obs_{LOS} \quad 0 \quad 0]^T
 \end{aligned} \tag{12}$$

The variables α_{az} and α_{inc} denote the azimuth and incidence angles, respectively, of the corresponding SAR observations. The observation of LOS deformation obtained from InSAR is represented as obs_{LOS} . It is important to note that in KFI-4D, the inclusion of temporal constraints in STE leads to the utilization of multiple interferometric phases from different interferogram pairs at a given time i as observations. Consequently, a design matrix is required to establish connections between the observations derived from various interferogram pairs. Assuming that the SAR observation at time i , along with its preceding n SAR observations, forms M interferogram pairs ($M < n$, with interferograms having large spatiotemporal baselines excluded), where the SAR observation at time i serves as the secondary image, the design matrix h_{ifg} can be mathematically expressed as follows:

$$h_{ifg} = \begin{bmatrix} -1 & 0 & 0 & \dots & 1 \\ 0 & -1 & 0 & \dots & 1 \\ \vdots & \vdots & \vdots & \ddots & \vdots \\ 0 & 0 & -1 & \dots & 1 \end{bmatrix} \tag{13}$$

where 1 denotes the epoch of primary SAR image observation, while -1 represents the epoch of secondary SAR image observation. By combining Equations 12 and 13, the system observation matrix L can be expressed as

$$\begin{aligned}
 L &= HX_i \\
 &= [h_{ifg} \otimes h_e \quad h_{ifg} \otimes h_n \quad h_{ifg} \otimes h_v][X_{e,i} \quad X_{n,i} \quad X_{v,i}]^T
 \end{aligned} \tag{14}$$

Here, \otimes denotes the Kronecker product operator.

In addition to the system observation matrix L , the SUE also requires the Kalman filter gain matrix. Based on Equation 1, the Kalman filter gain matrix K_κ is determined not only by the projection vector H but also by the variance-covariance matrices of the predicted value $D_{\hat{X}_i}^-$, the observation noise D_L , and the previous estimate $D_{\hat{X}_{i-1}}$. Among these matrices, the variance-covariance matrix of the predicted value $D_{\hat{X}_i}^-$ is calculated using the state transition vector F , the previous estimate's variance-covariance matrix $D_{\hat{X}_{i-1}}$, and the state transition variance-covariance matrix Q . The computation of the state transition variance-covariance matrix Q typically involves adaptive estimation, utilizing the state transition matrix and the observation model as follows:

$$Q_i = (1 - d(i)) \cdot Q_{i-1} + d(i) \cdot [K_{\kappa,i} v_i v_i^T K_{\kappa,i}^T + \hat{D}_{X,i} - F \hat{D}_{X,i-1} \cdot F^T] \tag{15}$$

where v_i represents the difference between the estimated deformation value \hat{X}_i and the observed value L , and $d(i)$ is the adaptive factor, which can be expressed as:

$$d(i) = \frac{(1 - b)}{(1 - b^i)}, 0 < b < 1 \tag{16}$$

It should be noted that the calculation of the variance-covariance matrix Q is performed after each completion of the Kalman filter dynamic estimation. At this time, the newly obtained state transition variance-covariance matrix Q_i will be used as Q_{i-1} in the next epoch's estimation.

During the calculation process of the Kalman filter gain matrix K_k , it is necessary to utilize the observation noise variance-covariance matrix D_L , which represents the observation noise associated with the system observation matrix L . Typically, this matrix can be derived from coherence. However, in the present method, the observations comprise unwrapped interferograms, which may include outliers such as unwrapped errors and decorrelation noise. To mitigate the influence of outliers, KFI-4D incorporates the Huber weight equation as a variance amplification model (Yang et al., 2002). Specifically, assuming that the observation noise variance-covariance matrix obtained directly from coherence at time i is denoted as $D_{L_{cc,i}}$, the observation noise variance-covariance matrix $D_{L,i}$ can be expressed using a variance amplification model as follows:

$$D_{L,i} = \begin{cases} D_{L_{cc,i}} & |\mu| < c \\ D_{L_{cc,i}} \cdot \frac{|\mu|}{c} & |\mu| > c \end{cases}, 1.0 < c < 1.5 \quad (17)$$

where c is a constant and μ represents the normalized residual of the observation matrix, which can be obtained from the following equation (J. Hu et al., 2013):

$$\mu = \frac{v_i}{\sqrt{D_{L_{cc,i}} + HD_{\hat{x},i}^-H^T}} \quad (18)$$

The Kalman filter gain matrix K_k is central to the Kalman filtering technique. At each time step, it achieves the optimal estimation of the state vector by determining the optimal weighting coefficient between the predicted state vector and the observed measurements (Kalman, 1960). The principle behind estimating the optimal weighting coefficient in the Kalman filter gain matrix is to minimize the covariance of the estimation error. By taking the derivative of the estimation error covariance matrix and minimizing it, the expression for K_k in Equation 1 can be derived. Therefore, using the variance-covariance matrix of the predicted state $D_{\hat{x},i}^-$, the variance-covariance matrix of the measurement noise D_L , the variance-covariance matrix of the previous estimate $D_{\hat{x},i-1}$, and the design matrix H , the Kalman filter gain matrix K_k can be obtained.

3.3. Implementation Instruction for KFI-4D Method

The workflow of KFI-4D is shown in Figure 2. Although STE and SUE are the core of the KFI-4D method, as shown in Equation 1, the predicted values, estimated values, and their variance-covariance matrix are continuously iterated throughout the process. Therefore, before implementing the KFI-4D method, it is necessary to obtain initial state vectors to initialize the Kalman filter process. This section starts with the raw input data and introduces the workflow of KFI-4D.

In terms of input data, KFI-4D requires SAR/InSAR observations acquired with at least two different imaging geometries as well as a digital elevation model (DEM). Here, data sets with different imaging geometries should exhibit significant differences in heading angles (e.g., ascending and descending tracks), incidence angles (e.g., adjacent tracks or different platforms), and looking angles (e.g., left- and right-looking modes). The DEM is not only used for removing the elevation phase in DInSAR processing but also used for spatial constraints in STE and SUE. In addition, considering that landslides generally occur in areas with severe spatiotemporal decorrelation, in order to suppress these decoherence noises, DInSAR processing requires selecting interferometric pairs with small spatiotemporal decorrelation based on a spatiotemporal baseline threshold as the input data for KFI-4D.

In terms of data preprocessing, KFI-4D requires the use of initial state vectors to obtain the initial 4-D movements at the first n epochs. As shown in Equation 4, STE requires the estimate of former n epochs to be the temporal constraints. However, this cannot be achieved for the initial n epochs. Therefore, in the processing of the initial n epochs in KFI-4D, the traditional KFI method will be used for temporal constraints (J. Hu et al., 2013) combined with the spatial constraints in Equation 2 to obtain the initial 4-D movements. In the process of using the traditional KFI method, it is generally necessary to obtain the 3-D deformation rate and its variance-covariance

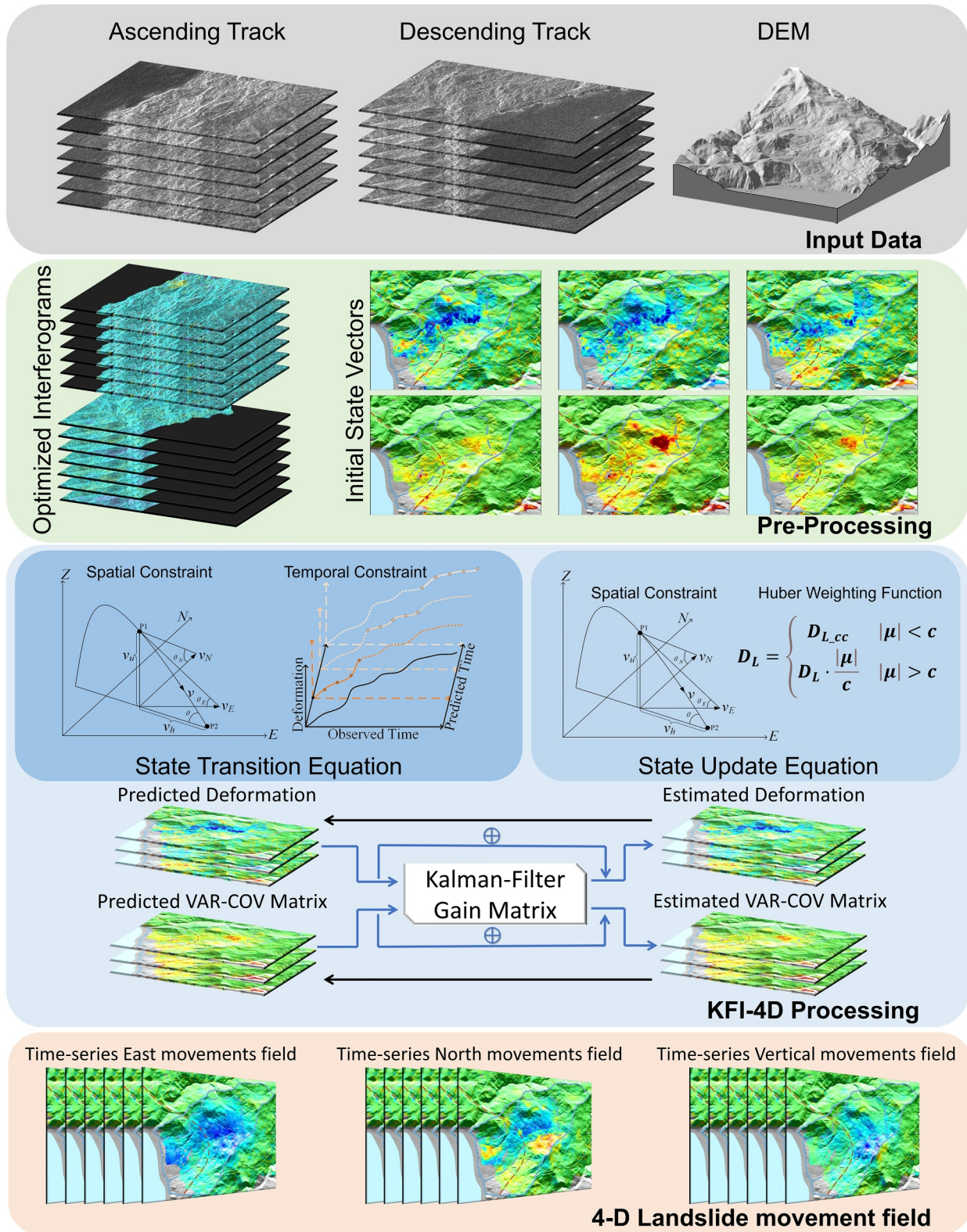


Figure 2. Schematic overview of the employed methods in this study. For detailed information on each step, please refer to Section 3.

matrix to initialize the KFI method (J. Hu et al., 2013). In this study, the SBAS method is used to obtain landslide movement rates on different orbits, and then combined with the surface parallel flow-constrained strain model (SPFS) (Zheng et al., 2023) to obtain the 3-D movement rates and their variance-covariance matrix for the landslide, which are used for the initialization of the KFI method. It should be noted that in the process of SBAS processing, in addition to obtaining landslide movement rates on different orbits, it is also possible to obtain elevation residuals in interferograms. Therefore, in order to suppress the effects of elevation residuals on the KFI-4D method, the elevation residuals obtained from the SBAS process will be used to remove the elevation residual phase in the original DInSAR interferometric phase during data preprocessing, reducing the impact of elevation residuals on the KFI-4D method.

In the processing of 4-D movements, KFI-4D first uses the initial state vector obtained during preprocessing to estimate the initial 4-D movements at the first n epochs based on the processing flow of the traditional KFI method combined with the spatial constraint in Equation 2. Then, using the spatiotemporal constraint in Equation 10, STE predicts the 4-D movement at the next i^{th} time and calculates its corresponding variance-covariance matrix using Equations 15 and 16. Next, KFI-4D calculates the variance-covariance matrix of the observation D_L using Equations 17 and 18 along with the variance-covariance matrix of the previous estimated value, the predicted value, and the projection vector H , and then uses Equation 1 to compute the Kalman filter gain matrix K_k . After that, KFI-4D updates the predicted value at i^{th} time using the Kalman filter gain matrix and the system observation L based on the spatial constraint SUE in Equation 11, obtaining the 3-D movements at i^{th} time. At the same time, using the Kalman filter gain matrix K_k , the projection vector H , and the variance-covariance matrix of the predicted value $D_{\hat{x},i}$, the variance-covariance matrix of the estimated value $D_{\hat{x},i}$ can be calculated, which will be used in the $(i + 1)^{\text{th}}$ of the Kalman filter dynamic processing flow to obtain the variance-covariance matrix of the predicted value and the Kalman filtering gain matrix for the next epoch. By following this process for each SAR observation epoch, the 4-D movements of the landslide can be obtained.

4. Results

4.1. Evaluation With Synthetic Data Sets

Compared to real data sets, synthetic data set allow for greater control over the influence of various factors on observations and enable the evaluation of computed results based on known correct outcomes. Thus, synthetic data sets will be utilized in this section to assess the performance of the KFI-4D method in obtaining 4-D movements and compare it with other methods. As noted in the introduction, current techniques for acquiring 4-D movements of landslides are limited to the UAVSAR synchronous observation method (X. Hu et al., 2020) and the Tikhonov regularization-based approach (e.g., MSBAS-3D) (Samsonov et al., 2020). However, the UAVSAR-based method is only applicable to UAVSAR environments and is unable to solve the under-determined problem caused by asynchronous observations in multi-platform SAR data fusion for obtaining 4-D movements. Moreover, its performance is equivalent to that of traditional 3-D movement acquisition. Therefore, this section mainly compares the KFI-4D method with the Tikhonov regularization-based method.

The procedure for generating the simulation is detailed in Text S1 of Supporting Information S1. Utilizing the 198 simulated interferograms from two orbits, both the Tikhonov regularization-based method and the KFI-4D method were employed to derive 4-D movements, which were subsequently compared with the simulated original signals. The outcomes are depicted in Figure S4 of Supporting Information S1. Overall, the deformation results acquired using both methods generally align with the landslide movement trend. However, concerning the time-series movement intricacies, the Tikhonov regularization-based method results display substantial fluctuations across all three deformation components, attributable to the impact of atmospheric and random noise (as denoted by the red dashed box in Figure S4 of Supporting Information S1). In contrast, the KFI-4D method yields more robust 4-D movements in terms of temporal evolution. Even under severe atmospheric and decorrelation noise, the movement results exhibited no significant fluctuations when compared with the simulated signal, thus more effectively revealing the landslide movement evolution process.

To quantify the disparities between the two methods, the results derived from the Tikhonov regularization-based method and the KFI-4D method were individually differentiated with the simulated signal, and the deviations were subjected to statistical analysis, as demonstrated in the histograms in Figure 3. It is evident that the Tikhonov regularization-based method significantly underestimates the eastward deformation component. As the LOS

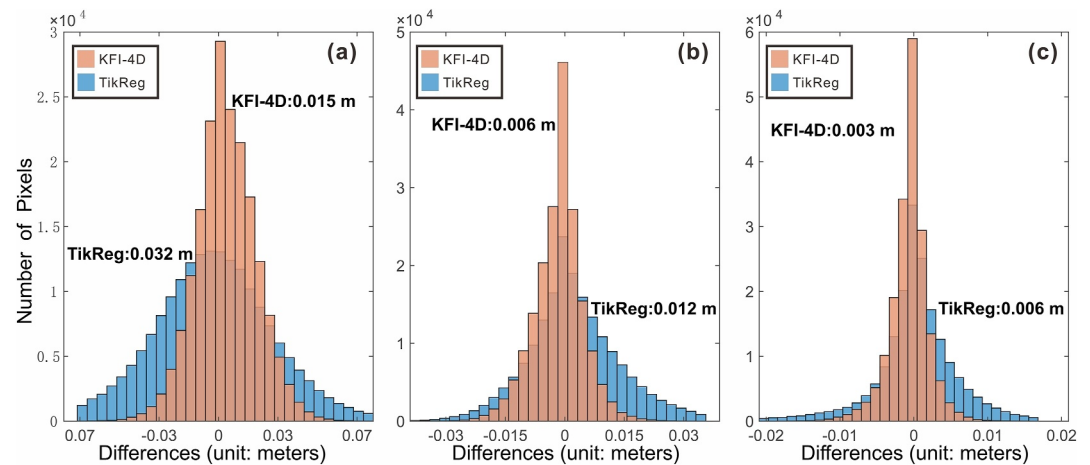


Figure 3. Comparative histograms displaying differences in 4-D movement results obtained using the KFI-4D method (orange columns) and the Tikhonov regularization-based method (blue columns) across three directions: (a) eastward, (b) northward, and (c) vertical.

deformation represents a projection of 3-D displacements, the northward and vertical deformation components are consequently overestimated. Taking into account the landslide movement direction, it becomes apparent that the deformation acquired using the Tikhonov regularization-based method underestimates the actual deformation. In comparison with the Tikhonov regularization-based method, the KFI-4D method markedly reduces the deviation of 4-D movements and outperforms the Tikhonov regularization-based method across all three components. Upon calculating the RMSEs for both methods, it emerges that the KFI-4D method attains RMSE values of 0.015, 0.006, and 0.003 m for the east, north, and vertical movement components, respectively. Relative to the deformation results procured using the Tikhonov regularization-based method, these values signify improvements of 53.1%, 48.3%, and 59.0%, respectively. Consequently, it can be deduced that the KFI-4D method effectively mitigates the influence of atmospheric and random noise, thereby enhancing the monitoring precision of 4-D landslide movements.

4.2. Applications to the Hooskanaden Landslide, Oregon

The Hooskanaden landslide is a large-scale landslide on the west coast of the US, which has persisted in a slow-moving state since its initial investigation in the early 1970s, experiencing multiple catastrophic events. To obtain the 4-D movements of the Hooskanaden landslide, we collected over 110 Sentinel-1A/B data from July 2016 to February 2019 before the catastrophic event occurred and processed them using KFI-4D. During data pre-processing, we set a 150 m spatial baseline and a 40-day temporal baseline for interferogram selection, with the final small baseline subset illustrated in Figure S5 of Supporting Information S1. However, it is worth noting that due to the adjustment of Sentinel-1A/B satellites, only four ascending SAR images were available from March–October 2018, as shown in Figure S5a of Supporting Information S1. This resulted in multiple InSAR subsets on the ascending track and also reduced the temporal resolution of InSAR monitoring. To remove the topographic phase, we used the 30 m COPDEM to remove the InSAR topographic phase during data processing. Subsequently, the data for the two orbits were processed according to the workflow shown in Section 3.3 and Figure 2, ultimately obtaining the 4-D movements of the Hooskanaden landslide, as depicted in Figure 4.

As shown in Figure 4a, the 3-D movement vectors indicate that the landslide predominantly moves southwest, with slow creep occurring at the toe, middle, and rear sections. The head exhibits a maximum movement rate of 142 mm/yr, and the toe shows 117 mm/yr. The middle section, traversed by US Highway 101, experiences significant deformation, reaching a maximum movement of approximately 100 mm/yr, which is smaller than the rear section. Contrary to the results by Xu et al. (2020), our findings suggest a more significant movement in the head and toe compared with the middle section. The discrepancy arises as Xu et al. (2020) primarily captured the motion during the February 2019 landslide event. Differential analysis using LiDAR DEMs from 2014 to 2008 confirmed significant deformation at the head and toe during the slow-moving stage (Xu et al., 2020), aligning with our observations. Field investigations reveal visible scarp in the middle and rear sections, along with fault

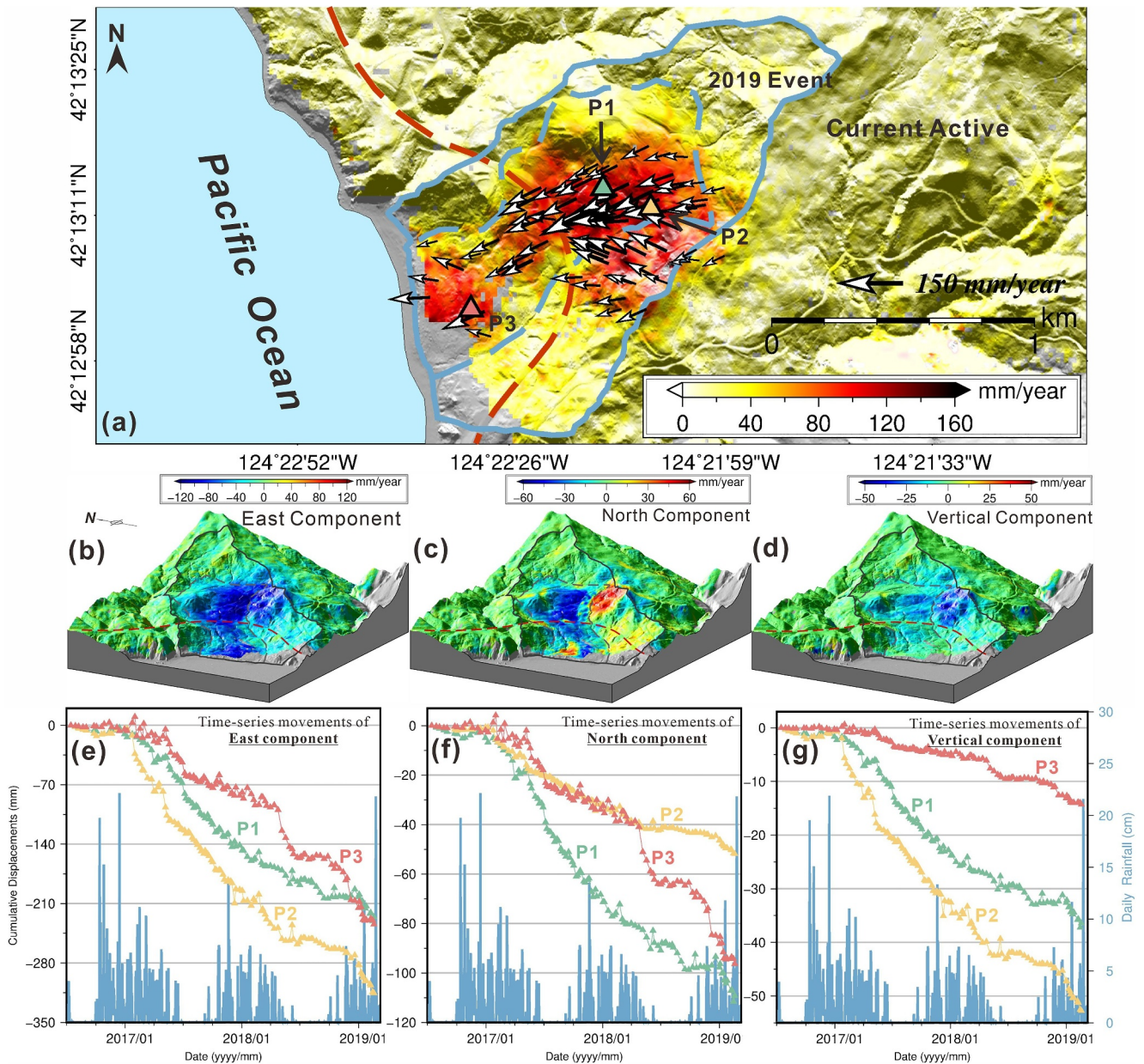


Figure 4. 4-D movements of the Hooskanaden landslide. (a) Vectors of the average 3-D movement rate, with arrows indicating the moving directions. The background shows a shaded relief map generated from a LiDAR DEM. (b)–(d) represent the 3-D movement rates of the east, north, and vertical components, respectively. (e)–(g) show the time-series 3-D movements at points P1–P3 during 15 July 2016 to 18 February 2019 with the same color triangles as in (a) used to illustrate their locations. The blue line represents the daily precipitation record obtained from a meteorological station (red mound) located 12 km away.

scarp and tension cracking at the rear (Alberti et al., 2020). The landslide movement occurred at the head and toe during slow creep, while the movement generated by landslide events mainly occurred in the middle section, indicating that the Hooskanaden landslide is controlled by multiple sliding surfaces (Xu et al., 2020). In the east, north, and vertical components, the maximum movement rates are -134 mm/yr, -56 mm/yr, and -39 mm/yr, respectively (Figures 4b–4d). The horizontal movement significantly surpasses the vertical movement, suggesting horizontal control, consistent with 3-D movement results derived from differential LiDAR DEM processing (Alberti et al., 2020). The gentle terrain likely contributes to the greater horizontal movement. The small vertical movement at the toe supports this observation.

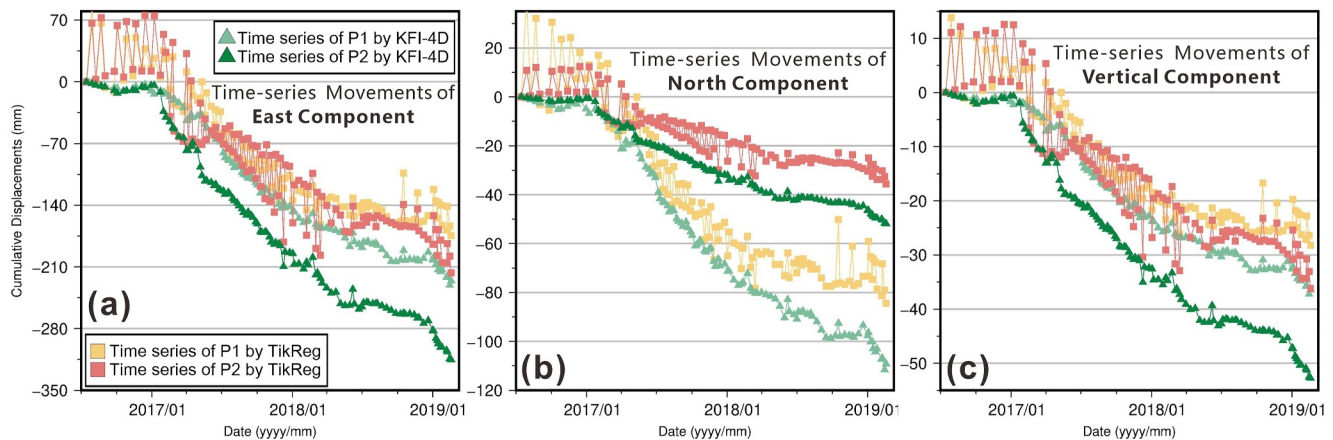


Figure 5. 4-D movements of the Hooskanaden landslide as determined by KFI-4D (represented by dark and light green triangles) and the Tikhonov regularization-based method (depicted by yellow and red squares) at locations P1 and P2 (refer to Figure 4a for their positions).

Three points (P1, P2, and P3) were selected at the head and toe sections, areas of pronounced landslide movement. Using the 4-D movement field, their time-series 3-D movement curves are plotted (Figures 4e–4g). The KFI-based 4-D Hooskanaden landslide movements enhance temporal resolution (J. Hu et al., 2013). Since the 4-D movements are derived from multiple track observations and processed using the KF dynamic process, compared to Xu et al.'s (2020) results from Sentinel-1 data of T13 track, our results overcame the data limitation in 2018. The missing data in T13 were supplemented by observations from T35. We obtained the movement details in 2018, capturing a notable acceleration before the February 2019 event. P1 and P2 on the rear section exhibited stability prior to the event, with significant acceleration at the end of 2018. Precipitation drove the Hooskanaden landslide (Xu et al., 2020), showing acceleration during wet seasons (from November to April of the following year). Different parts responded variably; P1 and P2 accelerated in the 2017 and 2019 wet seasons, while P3 at the toe reacted to the annual wet season with significant deformation in 2018. Despite higher rainfall in 2017, it did not lead to major disasters (Alberti et al., 2020). Rainfall alone inadequately explains landslide movement and the associated risks.

In order to compare the differences between KFI-4D and Tikhonov regularization-based methods in obtaining 4-D movements, the 4-D movements at points P1 and P2 were acquired and presented in Figure 5. It can be observed that the Tikhonov regularization-based method, like KFI-4D, can capture the overall deformation trend of the landslide. However, unlike the results obtained by KFI-4D, the Tikhonov regularization-based method exhibits significant fluctuations, especially in the initial epochs. These fluctuations are particularly evident in the time series of the eastward and vertical directions. Furthermore, influenced by these fluctuations, the cumulative displacement obtained by the Tikhonov regularization-based method displays a noticeable underestimation, which is similar to the outcomes derived from synthetic data sets. In comparison to the results obtained by the Tikhonov regularization-based method, KFI-4D effectively suppresses the impact of these fluctuations and acquires stable 4-D movements.

To quantify the differences in 4-D movements obtained by the Tikhonov regularization-based method and KFI-4D, the results obtained by these two methods were projected onto a third independent InSAR observation direction (e.g., the data set of Track 108) and used for comparison with the temporal LOS movements obtained by Track 108. It should be noted that the independent InSAR measurements obtained from the Track 108 data set have a temporal difference of only one day between the other two orbits. Therefore, these results are relatively suitable for comparison with the 4-D movements acquired in this study. Subsequently, 10 random points were selected on the Hooskanaden landslide, and the LOS temporal movements obtained by the three methods were compared (as shown in Figure S6 of Supporting Information S1). It can be observed that the results obtained by the Tikhonov regularization-based method also exhibit significant fluctuations in most points. In contrast, the KFI-4D results are closer to those obtained by the third independent InSAR observation. The RMSEs between the Tikhonov regularization-based method and KFI-4D results and the third independent InSAR observation results at these 10 random points are summarized in Table 1. The average RMS of KFI-4D at these 10 points is 6.2 mm, while the average RMS of the Tikhonov regularization-based method is 18.1 mm. Compared to the Tikhonov

Table 1
RMSEs Between the Time-Series LOS Movements Obtained From the Projections of the 4-D Movements Acquired by the Tikhonov Regularization-Based Method and KFI-4D Onto 10 Random Points, and the Time-Series LOS Movements Acquired From the Track 108 Data Set (Unit: mm)

Methods	pp1	pp2	pp3	pp4	pp5	pp6	pp7	pp8	pp9	pp10
TikReg	5.2	20.4	9.9	35.7	19.2	26.1	19.1	6.3	29.2	10.0
KFI-4D	3.4	3.9	4.8	5.2	6.5	7.9	6.0	6.5	9.3	8.0

regularization-based method, the improvement of KFI-4D reached 65.7%. Similarly, we calculated the RMS between the monitoring results obtained by the KFI-4D method and those from the Tikhonov regularization-based method with the Track 108 data sets for all pixels across the entire monitoring area (the statistical results are shown in Figure S7 of Supporting Information S1). The analysis shows that the average RMS of the KFI-4D method's results is only 23 mm, whereas, in contrast, the RMS from the Tikhonov regularization-based method reaches 135 mm. This statistical result indicates that, compared to the Tikhonov regularization-based method, the KFI-4D method can better suppress the influence of potential errors during the monitoring of landslide 4-D movements, thereby achieving more reliable 4-D movement measurements.

5. Discussions

5.1. The Superiority and Limitation of KFI-4D Method

The primary objective of KFI-4D is to address the underdetermined issue in the processing of 4-D movements and to obtain high-resolution 4-D movement fields of landslides using InSAR technology. The efficacy of the KFI-4D approach in mitigating monitoring noise in landslide monitoring and enhancing the accuracy of 4-D movements is illustrated through comparisons with conventional methods employing both real and synthetic data sets. During processing, KFI-4D necessitates the utilization of SAR observation data from diverse imaging geometries, which not only mitigates the ill-conditioned problem in InSAR monitoring (Zheng et al., 2023) and enhances monitoring accuracy but also improves the temporal resolution of InSAR monitoring since distinct imaging geometries possess varying observation times for landslides. Prior to the occurrence of catastrophic landslide events, landslides could exhibit significant acceleration signals (Xiong et al., 2020). Sentinel-1, an SAR satellite capable of routine global coverage, possesses a temporal resolution of approximately 12 days, rendering it insufficient for the rapid detection of landslide acceleration signals. Some satellites, such as Lutan-1 (LT-1) (Jin et al., 2020) and RADARSAT Constellation Mission (RCM) (Thompson, 2015), have enhanced the temporal resolution of InSAR to 4 days or even higher by forming satellite constellations. By implementing the KFI-4D method proposed in this study to jointly analyze Sentinel-1 observations with higher temporal resolution SAR satellite observations, it becomes feasible to not only acquire 4-D movements of landslides but also to further refine the temporal resolution of InSAR. Consequently, this will facilitate the timely detection and identification of abnormal acceleration signals of landslides, ultimately reducing potential casualties and property losses.

Moreover, during the acquisition of the 4-D movements of the Hooskanaden landslide using real data sets, the Sentinel-1 satellite adjustment influenced the availability of SAR observation images. Consequently, only 4 images were obtained on Track 35 between 15 March 2018, and 17 October 2018. This limitation not only reduced the temporal resolution of InSAR observations but also rendered many deformation details unobservable throughout 2018. As demonstrated by Xu et al. (2020)'s findings using Track 35 data, the deformation results derived solely from Track 35 SAR imagery during 2018 closely resembled a straight line, complicating the determination of changes in the Hooskanaden landslide movements during this period. In this study, the KFI-4D method, combined with Track 13 SAR data, successfully recovered the 4-D movements from March–October 2018 (as depicted in Figures 4e–4g). These results clearly illustrate the impact of rainfall on landslide movements during the 2018 wet season (November to April of the following year). In addition to temporary adjustments of SAR satellites, the failure of SAR satellites also contributes to InSAR's inability to continuously monitor specific targets. For instance, Sentinel-1B failed in December 2021, rendering its SAR images unavailable for future use in areas where it had been continuously observed. Specifically, the repeat interval in Europe has been significantly reduced from 6 to 12 days. Consequently, these areas will rely solely on Sentinel-1A for alternative coverage. In the foreseeable future, satellites such as NISAR (NISAR, 2018) and ALOS4 PALSAR3 (Kankaku et al., 2023) will be launched. Based on the KFI-4D method proposed in this study, observations from other SAR satellites can serve as a supplement in cases where a satellite (e.g., Sentinel-1B) becomes unavailable. This approach will help ensure the continuity of landslide monitoring.

However, it is important to note that KFI-4D incorporates the slope aspect as a constraint in both STE (Equation 10) and SUE (Equation 12). Similar to other SPF-based methods (Kang et al., 2023), when the slope aspect of

a landslide is oriented in the north-south direction, the state transition matrix F in STE and the projection vector H in SUE may experience matrix ill-conditioning, which significantly reduces the accuracy of 4-D movement estimations. The rationale behind introducing slope aspect constraints in KFI-4D is to enhance InSAR's sensitivity to north-south deformation (J. Hu et al., 2014). Pixel Offset Tracking (POT) (Michel et al., 1999) and Multiple Aperture InSAR (MAI) (Bechor & Zebker, 2006) are prevalent methods for obtaining azimuth deformation. If azimuth deformation can be determined using POT or MAI, the slope aspect constraint can be eliminated from STE and SUE, circumventing the ill-conditioning of the coefficient matrix induced by the slope aspect constraint and obtaining the 4-D movements of north-south landslides. However, for current Sentinel-1 data, the adoption of the TOPS imaging mode results in relatively low azimuth resolution, making it challenging to acquire azimuth deformation using Sentinel-1 data. Consequently, this approach is restricted to cases where high-resolution SAR data are accessible (e.g., TanDEM-X). Nevertheless, it is essential to highlight that future NISAR and ALOS4 PALSAR3 missions will offer higher azimuth resolution SAR images, and since the observations will be acquired in the L-band, coherence is expected to be significantly improved, especially in vegetated landslide areas. As such, it is valuable to further investigate the computation of landslide 4-D movements using KFI-4D in conjunction with azimuth deformation obtained from NISAR or ALOS4 PALSAR3.

Moreover, KFI-4D is not suitable for shallow landslides. The KFI-4D technique estimates 4-D landslide movements using data from InSAR, POT, or MAI methods. However, unlike the large landslides in the study area, shallow landslides, which are generally smaller in scale, often lack a significant slow-moving phase in their early stages. As a result, techniques such as InSAR, POT, or MAI typically fail to detect notable deformation signals, rendering KFI-4D ineffective. Similarly, KFI-4D has limited applicability for rockslides, which rarely exhibit a slow-moving phase. Furthermore, for small-scale slopes (length and width <100 m), even if some displacement occurs during rainfall, it is difficult to capture significant deformation signals with Sentinel-1 data due to its relatively low spatial resolution, leading to KFI-4D's failure. To address this issue, high-resolution data (such as TerraSAR/TanDEM-X or ALOS2 PALSAR2) could be employed to capture slope deformation; however, the feasibility of these data sets requires further testing.

5.2. The Effect of Slope Aspect on Estimated 4-D Movements

KFI-4D method incorporates terrain constraints similar to other SPF-constrained methods; therefore, the monitoring results are influenced by the slope aspect (Kang et al., 2023). In order to quantitatively evaluate the impact of slope aspect on the KFI-4D method, we simulated 3,650 synthetic data sets with different coherences and varying landslide aspects using the method described in Section 4.1. These data sets were then solved using the KFI-4D method to obtain the 4-D movements, and the RMSEs were calculated. The results shown in Figure 6 indicate that when the commonly used observation configuration of ascending track combined with descending track is used, an increase of 44° or 221° in the slope aspect of landslides (as indicated by the black dashed lines in Figure 6) significantly amplifies the RMSEs of the 4-D movements. Considering that the average slope aspect in the synthetic data sets is -43° , the KFI-4D method is unable to obtain reliable 4-D movements when the slope aspect is 1° or 178° due to matrix ill-conditioning, which is consistent with the findings of Kang et al. (2023). It is worth noting that this impact varies for the eastward, northward, and vertical components of the 4-D movements. The time-series movement results of the eastward component are most significantly affected, followed by the northward component, while the vertical component is least affected. However, for the northward component, apart from the tendency for higher RMSEs near slope aspects of 0° or 180° , low coherence levels also decrease the accuracy of solving the northward temporal movements when the slope aspect is near 90° (as indicated by the red dashed line in Figure 6).

The impact of slope aspect is not only evident in the potential for ill-conditioned coefficient matrices in terrain-constrained methods but also in the reduction of InSAR observation coherence (Kellndorfer et al., 2022), leading to monitoring blind zones due to terrain layover or shadowing effects (Cai et al., 2022). These blind zones often appear only in a certain direction of the orbit, while the other direction of the orbit remains unaffected by SAR layover or shadow. Therefore, it is possible to consider using InSAR observations from the same direction (e.g., two ascending orbits from different SAR satellites) to obtain 4-D movements. Here, we used a configuration of two ascending tracks to simulate 3,650 synthetic data sets with different coherences and varying slope aspects, in order to assess the impact of slope aspect on 4-D movements. As shown in Figure 6, when using two ascending tracks as the observation configuration, although there is a slight improvement in the temporal movement results of the vertical component, the RMSEs of the other two components significantly deteriorate. This also indicates

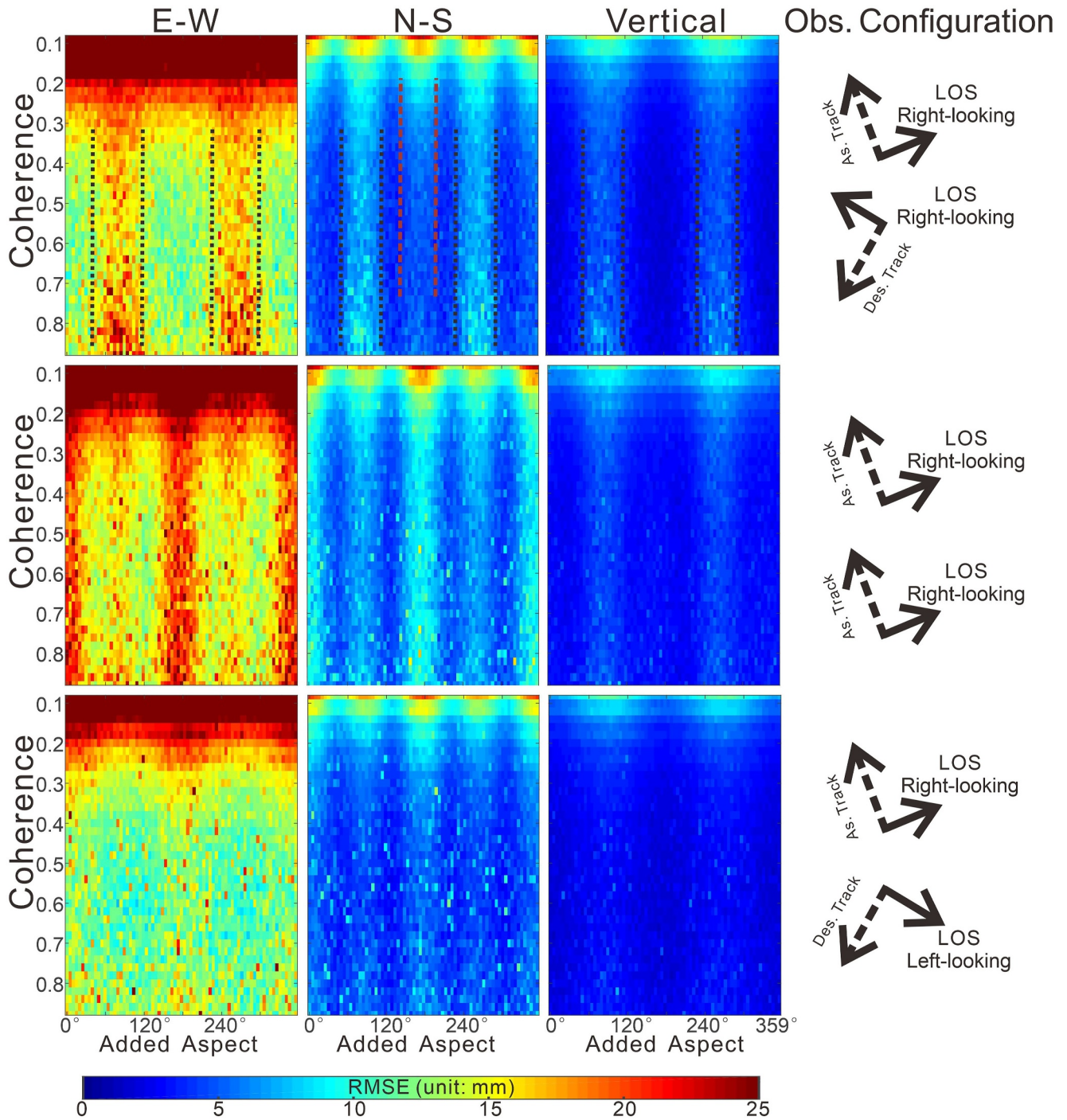


Figure 6. RMSEs of 4-D movements obtained using different InSAR observation configurations based on the KFI-4D method under different landslide slope aspect and coherence conditions. The X-axis represents the added slope aspect in the original slope direction, and the Y-axis represents coherence.

that using SAR observation data sets from the same flight direction can effectively address the issue of blind zones caused by layover and shadowing, but due to the similar geometries of satellite observations from the same flight direction, it further weakens the monitoring accuracy of 4-D movements.

Left-looking SAR observations are a novel SAR observation strategy that can effectively improve the results of 3D deformation monitoring (Zheng et al., 2023). When left-looking SAR and right-looking SAR are combined to observe a target from one direction, there are also imaging geometric differences between the two observation

data sets, which provides an opportunity to improve the inability to use two LOS observations to obtain 4-D movements due to layover or shadow. To this end, we used a configuration of right-looking SAR from one ascending track and left-looking SAR from one descending track as the observation setup to simulate 3,650 synthetic data sets with different coherences and varying slope aspects, in order to assess the impact of slope aspect on 4-D movements. The results, as shown in Figure 6, demonstrate that the combination of right-looking SAR and left-looking SAR significantly improves the RMSEs of 4-D movements compared to the other two observation configurations. Under the condition of coherence greater than 0.3, the impact of slope aspect on 4-D movements is reduced to within 10 mm. Even when the slope aspect is at 0° or 180° , the RMSE of the eastward component is less than 15 mm. Therefore, this also indicates the potential of using left-looking SAR observations in conducting 4-D movements. In the upcoming SAR missions, both NISAR and ALOS4 PALSAR3 are equipped with left-looking observation modes. Especially for NISAR, in order to improve the coverage in the Antarctic region, it will use the left-looking observation mode in most regions (NISAR, 2018). This will provide an opportunity to mitigate the impact of the slope aspect on the solution of 4-D movements in the future, and help further expand the application scenarios of 4-D movements based on InSAR technology.

Furthermore, it is noteworthy that the European Space Agency (ESA) is planning to develop a novel InSAR Earth observation mode based on the Harmony mission to capture 3-D surface deformation (Dekker et al., 2019). This plan involves the use of two additional satellites, Harmony-A and Harmony-B, in conjunction with the future Sentinel-1C or Sentinel-1D satellites. Sentinel-1C/D will act as the illuminator, while Harmony-A/B will function as a receive-only satellite (Dekker et al., 2019). By utilizing this innovative joint observation mode, the Harmony mission is also expected to overcome the effects of the slope aspect, enabling the acquisition of 4-D surface deformation.

5.3. Blocks Interaction Dynamics Revealed by InSAR-Derived 4-D Movements

Landslide movement often involves the interaction of multiple blocks rather than a single mass moving independently (Ferrari et al., 2011; Tomás et al., 2014). The combined effects of these blocks can lead to either accelerated or stable landslide behavior. Therefore, investigating the interaction dynamics between multiple blocks during landslide movement holds significant importance in gaining a deeper understanding of landslide mechanisms and facilitating early warning and mitigation efforts. However, the interaction of multiple blocks can introduce complexity in landslide modeling and research (Ferrari et al., 2011). Traditional field observation methods only provide sparse measurements of the landslide with low spatial resolution, limiting the ability to achieve comprehensive observations of landslides.

Strain is a measure of deformation experienced by an object under external forces. By using strain tensors, we can derive multiple strain invariants, which serve as essential tools for understanding the interaction between different blocks (Mehrabi, 2021). Utilizing the proposed KFI-4D, the 4-D movements of the Hooskanaden landslide were derived using ascending and descending Sentinel-1 data acquired between July 2016 and February 2019 prior to the occurrence of the catastrophic event. This enables us not only to calculate the strain invariants from the 3-D movements but also to further explore the dynamics of strain invariants based on the 4-D movements (further details regarding the calculation of strain invariants from the obtained 4-D movements are provided in Text S2 of Supporting Information S1). Here, the dynamics of dilatation and maximum shear strain of the Hooskanaden landslide are derived as a medium to further investigate the block interaction dynamics preceding the catastrophic event.

5.3.1. 4-D Movements-Derived Dilatation Dynamics

The Hooskanaden landslide's 3-D movement rate allows the inversion of strain invariants. Figure 7a presents the calculated dilatation rate field derived from the 3-D movement rate via Equation S5 of Supporting Information S1, revealing distinct blocks based on dilatation patterns. The Hooskanaden progress report defines Internal Scarps (IS) positions marking blocks and profile A-A' (Parker, 1979). Extracting dilatation results along profile A-A' and comparing them to IS positions (Figure 7b), we find a maximum dilatation rate of $2.1 \times 10^{-3}/\text{yr}$ and minimum compression rate of $-1.3 \times 10^{-3}/\text{yr}$ along section A-A'. Notably, IS1, IS3, IS4, and IS5 exhibit alternating dilatation and compression. Hence, these IS positions demarcate block boundaries. Most prominently, IS3 and IS4 show significant variations. At IS3, the compression rate increases from $-1.1 \times 10^{-3}/\text{yr}$ to $1.4 \times 10^{-3}/\text{yr}$, and at IS4, the dilatation rate decreases from $1.7 \times 10^{-3}/\text{yr}$ to $-0.8 \times 10^{-3}/\text{yr}$. In contrast, unlike the

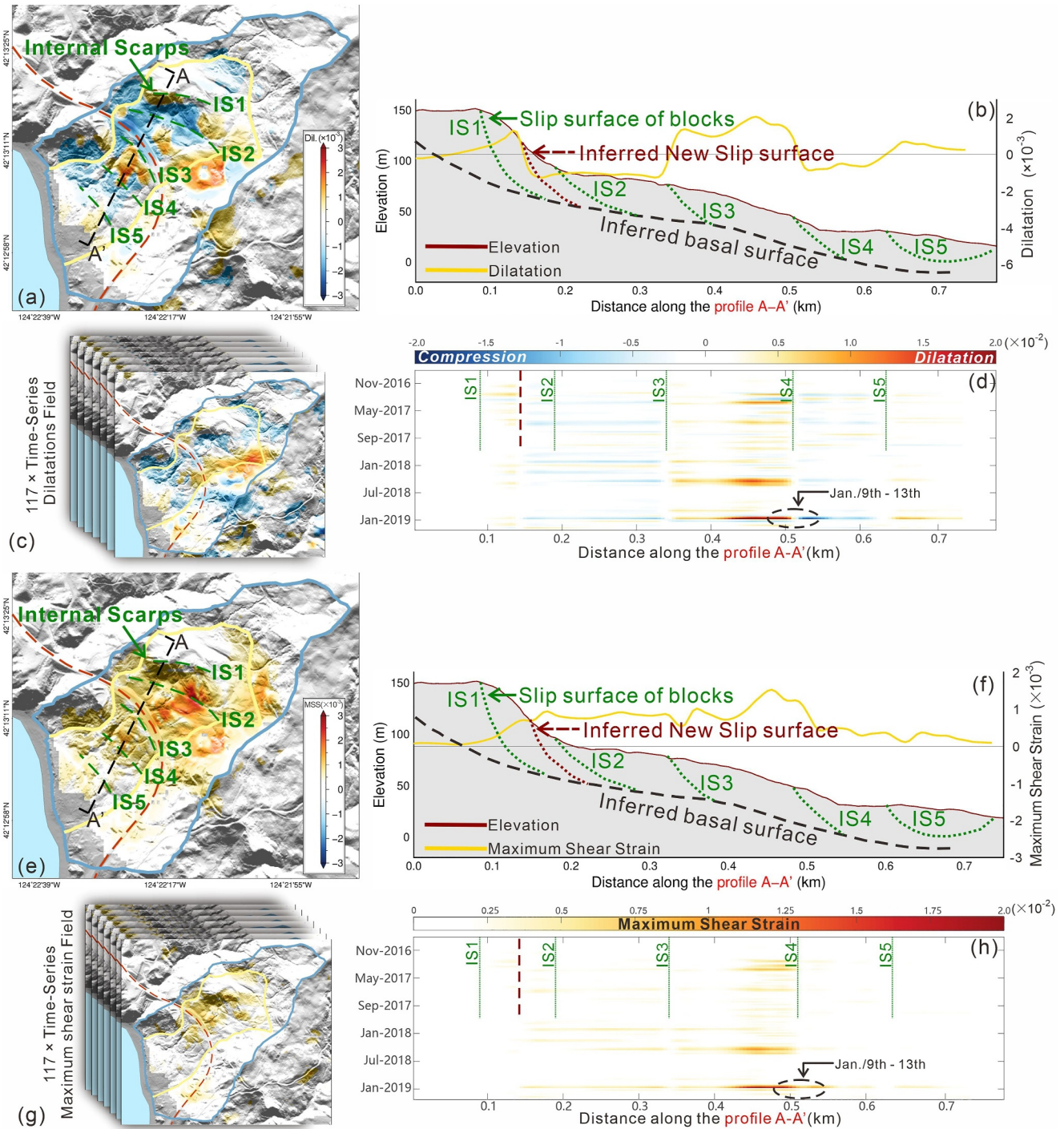


Figure 7. Strain invariant fields derived from the movement rates. Panels (a) and (e) show dilatation and MSS rate fields, respectively, plotted on the LiDAR DEM-generated shaded relief map. The black and green dashed lines indicate the locations of the profile and internal scarps, respectively, extracted from the progress report of the Hooskanaden landslide (Parker, 1979). Panels (b) and (f) present the dilatation and MSS rates along profile A-A', respectively, with elevation and inferred basal surface information sourced from the progress report (Parker, 1979). Panels (c) and (g) illustrate the time-series movements-derived transient dilatation and MSS fields, respectively. Panels (d) and (h) display the time-series transient dilatation and MSS rate along profile A-A', respectively. The strain invariant fields are all dimensionless.

Hooskanaden report, our results show minimal dilatation differences near IS2, suggesting that it might not be a block boundary. Instead, a substantial dilatation difference was observed between IS1 and IS2, resulting in a sudden decrease from $1.2 \times 10^{-3}/\text{yr}$ to $-1.3 \times 10^{-3}/\text{yr}$. This leads us to hypothesize that this discrepancy could

potentially signify the presence of a novel slip surface, indicated by the red dashed line in Figure 7b. The existence and distribution of distinct blocks within the Hooskanaden landslide explain differences in our results compared with those of Xu et al. (2020). Notably, Figure 7a's dilatation rate field shows substantial dilatation in the middle section, reaching the maximum dilatation rate of $2.1 \times 10^{-3}/\text{yr}$. This block accumulates stress during the prolonged slow-moving process, possibly explaining significant movement during the February 2019 event.

Utilizing the 4-D movement field, we derived the time-series transient dilatation rate field of the Hooskanaden landslide (Figure 7c). We also extracted time-series transient dilatation along profile A-A' (Figure 7d), revealing a distinct boundary between blocks. Like the results in Figure 7b, the transient dilatation rate along A-A' does not exhibit a demarcation line at IS2, but a prominent boundary emerges on the inferred new slip surface. These observations affirm that IS1, IS3, IS4, IS5, and the inferred new slip surface indeed serve as boundaries between distinct blocks, while IS2 no longer functions as a slip surface. Long-term movement and the occurrence of catastrophic events spanning decades could be responsible for this shift in IS2's role as a slip surface. Friction along the slip surface stands as a critical parameter governing block movement rate and stability (W. Hu, Huang, et al., 2019). In the event of a catastrophic incident, the rapid movement of a sizable mass of landslide material may initiate a series of friction-reducing mechanisms on the slip surface, such as thermal decomposition of basal carbonates (Anders et al., 2000) or recrystallization (W. Hu, Huang, et al., 2019). The catastrophic events witnessed in the Hooskanaden landslide over the past few decades might have triggered friction-reducing mechanisms. Consequently, the friction on the slip surface decreased, leading to IS2's transition from a slip surface.

Temporal dilatation patterns show blocks mostly sustain a consistent trend of dilation or compression throughout the observation period, influenced by adjacent blocks (Figure 7d). When the central block experiences dilatation, adjacent blocks exhibit compression, and vice versa. However, distinct blocks do not always follow a uniform pattern over time (Figure 7d). Changes can swiftly transition from dilatation to compression or vice versa, affecting adjacent blocks. As an illustration, consider the block positioned between IS3 and IS4. Over the observation period, the predominant trend was dilation, with a notable maximum transient dilation rate of $2.4 \times 10^{-2}/\text{yr}$. However, there are instances where it momentarily shifts to compression, with the lowest transient compression rate recorded at $-0.8 \times 10^{-2}/\text{yr}$. The dilatation boundary of each block exhibits relative stability throughout the time series without crossing the slip surface. This underscores that during the slow-moving phase, block movements are not controlled by a single basal surface but by multiple slip surfaces. For instance, at IS5, dilatation sometimes crosses the boundary (Figure 7d). Parker (1979) reported that IS5 does not intersect the inferred basal surface. This discrepancy may explain why the block in that area is intermittently influenced by the basal surface.

5.3.2. 4-D Movements-Derived Maximum Shear Strain Dynamics

The Maximum Shear Strain (MSS) rate field of the landslide can be derived using Equation S6 of Supporting Information S1, as depicted in Figures 7e and 7f. The time-series transient MSS rate obtained from the 4-D movement field offers a novel perspective on comprehending the landslide's motion dynamics (Figures 7g and 7h). Similar to the time-series dilatation results, the temporal MSS pattern also reveals distinct boundaries among various blocks, aligning with the distribution of boundaries observed in the dilatation field. However, it's notable that the boundaries in the temporal MSS pattern appear somewhat blurred compared to those identified in the dilatation field. This phenomenon arises due to the interconnectedness of adjacent blocks' MSS when significant MSS values emerge. The region displaying the most pronounced dilatation and MSS within the landslide is the block positioned between IS3 and IS4. Remarkably, this block's location corresponds to where the most extensive movement occurred during the February 2019 event. Temporal analysis of the time-series transient MSS rate revealed a substantial annual increase in MSS for this block during the wet season (November to April of the following year, Figure 7h), accompanied by noteworthy dilatation (Figure 7d). This emphasizes that both MSS and the dilatation field of the Hooskanaden landslide exhibit considerable sensitivity to rainfall, paralleling the findings of Xu et al. (2020). Particularly significant is the observation that one month before the February 2019 event, specifically from January 9th to 13th, the most prominent dilatation and MSS during the observation period were evident (marked by black dashed circles in Figures 7d and 7h). The maximum transient dilatation rate surged to $2.4 \times 10^{-2}/\text{yr}$, while the peak transient MSS rate escalated to $1.8 \times 10^{-2}/\text{yr}$. Remarkably, this timeframe witnessed a pronounced interconnection between the MSS of the central block and its neighboring blocks, with the transient MSS rate of the adjacent block also reaching $0.9 \times 10^{-2}/\text{yr}$. This phenomenon has the potential to be a significant causal factor and a pivotal indicator leading to the onset of the February 2019 event.

It is noteworthy that the variation in landslide friction occurs not only during high-speed movements of landslides but also during the slow-moving phase (Zhang et al., 2023). When the effect of pore-water pressure sufficiently counteracts the friction-strengthening influence, friction weakening arises. This phenomenon can propel the landslide's movement velocity beyond its potential upper limit, resulting in disasters (Zhang et al., 2023). The abnormal signals in transient MSS and dilatation rate observed between January 9th and 13th could illustrate this process. Exploring this process in-depth will contribute to improved landslide early warning systems. However, a comprehensive understanding of the mechanics underlying abnormal signal action necessitates the integration of more in situ testing data and subsurface field observations (Ye et al., 2024a, 2024b).

6. Conclusions

The utilization of InSAR-derived 4-D movements as a high-resolution and intuitive product for monitoring landslides greatly contributes to the advancement of our understanding and research in this field. In this study, we propose the KFI-4D method by enhancing the state transfer equation and state update equation of the Kalman filter and incorporating spatiotemporal constraints. This method effectively addresses the challenge of under-determination in obtaining 4-D movements and broadens the application scope of InSAR technology for acquiring 4-D movements. Synthetic data sets and the practical application results of the Hooskanaden landslide demonstrate that the KFI-4D method successfully mitigates the influence of InSAR observation errors during the acquisition of 4-D movements. Compared to the conventional Tikhonov regularization-based method, the KFI-4D method showcases a remarkable improvement of over 50% in terms of RMSE. Moreover, the KFI-4D method dynamically estimates parameters during computation, enabling the incorporation of SAR observations from other orbits to supplement continuous landslide monitoring tasks and enhance temporal resolution. Regarding the potential limitations of using terrain as a constraint in the implementation of the KFI-4D method, we evaluated the impact of terrain on estimated 4-D movements using synthetic data sets. Our findings reveal that when acquiring 4-D movements through ascending and descending track data, the east and north components of the movements fail to produce reliable results when the slope aspect reaches 0° or 180°. However, when examining the influence of slope aspect on the acquisition of 4-D movements using left-looking data, we discover that the KFI-4D method effectively overcomes the impact of slope aspect and obtains dependable 4-D movements when introducing left-looking data with a coherence greater than 0.3. Considering the upcoming adoption of a left-looking mode by the NISAR satellite, the future application and monitoring performance of the KFI-4D method hold great promise for further enhancements.

By utilizing the KFI-4D method and Sentinel-1A/B data from ascending and descending tracks, we successfully obtained the 4-D movements of the Hooskanaden landslide from July 2016 to the catastrophic event in February 2019. Our findings highlight variations in the response of different sections of the landslide to rainfall. Leveraging high-resolution 4-D movement data, we inferred the strain invariants dynamics of the landslide: (a) The distribution and activity of blocks and slip surfaces can be assessed; (b) Whether the kinematics of distinct blocks are governed by autonomous slip surfaces or a common basal surface can be assessed; (c) The sensitivity of various blocks to the trigger can be evaluated, with anomalous strain invariant signals potentially serving as vital indicators for landslide early warning before potential catastrophic events. Future satellites such as NISAR, ALOS4 PALSAR3, and Sentinel-1C hold the promise of providing additional InSAR observations for landslide dynamics research. Implementing the KFI-4D method based on these advancements can further improve the temporal resolution of InSAR-based landslide monitoring. Consequently, this advancement has the potential to enable the identification of abnormal signals in strain invariants prior to the occurrence of catastrophic events, thereby facilitating efforts in landslide early warning.

Data Availability Statement

Sentinel-1 SAR data sets can be downloaded from the Alaska Satellite Facility <https://search.asf.alaska.edu/>. For Sentinel-1 ascending data set, search for "L1 SLC" File Type, "IW" Beam Mode, "Ascending" Direction, Path #35 and Frame #137. For Sentinel-1 descending data set, search for "L1 SLC" File Type, "IW" Beam Mode, "Descending" Direction, Path #13 and Frame #453. The Copernicus DEM and LiDAR DEM are available through <https://opentopography.org/>; choose "FIND DATA MAP" from the "DATA" menu and then enter the minimum and maximum latitude and longitude as in Figure 1. The Copernicus DEM is collected in "Global and Regional DEM" catalog, and the LiDAR DEM is collected in "NOAA" catalog.

Acknowledgments

We thank Editor Mikael Attal, Associate Editor Matt Brain, Dr. Qi Ou, and the anonymous reviewer for their insightful comments. The research was supported by the National Natural Science Foundation of China under Grant 42030112, the Science and Technology Innovation Program of Hunan Province under Grant 2022RC3042, the Nature Science Foundation of Hunan Province under Grant 2022JJ30031, and the Research Grants Council of the Hong Kong SAR Government under the Theme-based Research Scheme (T22-606/23-R).

References

Alberti, S., Senogles, A., Kingen, K., Booth, A., Castro, P., DeKoekoek, J., et al. (2020). The Hooskanaden landslide: Historic and recent surge behavior of an active earthflow on the Oregon coast. *Landslides*, 17(11), 2589–2602. <https://doi.org/10.1007/s10346-020-01466-8>

Anders, M. H., Aharonov, E., & Walsh, J. J. (2000). Stratified granular media beneath large slide blocks: Implications for mode of emplacement. *Geology*, 28(11), 971–974. [https://doi.org/10.1130/0091-7613\(2000\)28<971:sgmbls>2.0.co;2](https://doi.org/10.1130/0091-7613(2000)28<971:sgmbls>2.0.co;2)

Bechor, N. B. D., & Zebker, H. A. (2006). Measuring two-dimensional movements using a single InSAR pair. *Geophysical Research Letters*, 33(16). <https://doi.org/10.1029/2006gl026883>

Cai, X., Chen, L., Xing, J., Xing, X., Luo, R., Tan, S., & Wang, J. (2022). Automatic extraction of layover from InSAR imagery based on multilayer feature fusion attention mechanism. *IEEE Geoscience and Remote Sensing Letters*, 19, 1–5. <https://doi.org/10.1109/LGRS.2021.3105722>

Dalaison, M., & Jolivet, R. (2020). A Kalman filter time series analysis method for InSAR. *Journal of Geophysical Research: Solid Earth*, 125(7), e2019JB019150. <https://doi.org/10.1029/2019jb019150>

Dekker, J. F., Lopez, B., Juliet, Chapron, B., Hooper, A., Kääh, A., et al. (2019). The Harmony mission: Applications and preliminary performance. In *Paper Presented at the 6th Workshop on Advanced RF Sensors and Remote Sensing Instruments*. ARSI'19.

Ferrari, A., Ledesma, A., González, D. A., & Corominas, J. (2011). Effects of the foot evolution on the behaviour of slow-moving landslides. *Engineering Geology*, 117(3–4), 217–228. <https://doi.org/10.1016/j.enggeo.2010.11.001>

Handwerger, A. L., Booth, A. M., Huang, M.-H., & Fielding, E. J. (2021). Inferring the subsurface geometry and strength of slow-moving landslides using 3-D velocity measurements from the NASA/JPL UAVSAR. *Journal of Geophysical Research: Earth Surface*, 126(3). <https://doi.org/10.1029/2020jef005898>

Handwerger, A. L., Huang, M. H., Fielding, E. J., Booth, A. M., & Burgmann, R. (2019). A shift from drought to extreme rainfall drives a stable landslide to catastrophic failure. *Scientific Reports*, 9(1), 1569. <https://doi.org/10.1038/s41598-018-38300-0>

Hu, J., Ding, X.-L., Li, Z.-W., Zhu, J.-J., Sun, Q., & Zhang, L. (2013). Kalman-filter-based approach for multisensor, multitrack, and multi-temporal InSAR. *IEEE Transactions on Geoscience and Remote Sensing*, 51(7), 4226–4239. <https://doi.org/10.1109/tgrs.2012.2227759>

Hu, J., Ding, X.-L., Zhang, L., Sun, Q., Li, Z.-W., Zhu, J.-J., & Lu, Z. (2017). Estimation of 3-D surface displacement based on InSAR and deformation modeling. *IEEE Transactions on Geoscience and Remote Sensing*, 55(4), 2007–2016. <https://doi.org/10.1109/tgrs.2016.2634087>

Hu, J., Li, Z., Ding, X., Zhu, J., Zhang, L., & Sun, Q. (2014). Resolving three-dimensional surface displacements from InSAR measurements: A review. *Earth-Science Reviews*, 133, 1–17. <https://doi.org/10.1016/j.earscirev.2014.02.005>

Hu, W., Huang, R., McSaveney, M., Yao, L., Xu, Q., Feng, M., & Zhang, X. (2019). Superheated steam, hot CO2 and dynamic recrystallization from frictional heat jointly lubricated a giant landslide: Field and experimental evidence. *Earth and Planetary Science Letters*, 510, 85–93. <https://doi.org/10.1016/j.epsl.2019.01.005>

Hu, X., Bürgmann, R., Lu, Z., Handwerger, A. L., Wang, T., & Miao, R. (2019). Mobility, thickness, and hydraulic diffusivity of the slow-moving monroe landslide in California revealed by L-band satellite radar interferometry. *Journal of Geophysical Research: Solid Earth*, 124(7), 7504–7518. <https://doi.org/10.1029/2019jb017560>

Hu, X., Bürgmann, R., Schulz, W. H., & Fielding, E. J. (2020). Four-dimensional surface motions of the Slumgullion landslide and quantification of hydrometeorological forcing. *Nature Communications*, 11(1), 2792. <https://doi.org/10.1038/s41467-020-16617-7>

Jin, G., Liu, K., Liu, D., Liang, D., Zhang, H., Ou, N., et al. (2020). An advanced phase synchronization Scheme for LT-1. *IEEE Transactions on Geoscience and Remote Sensing*, 58(3), 1735–1746. <https://doi.org/10.1109/tgrs.2019.2948219>

Joughin, I. R., Kwok, R., & Fahnestock, M. A. (1998). Interferometric estimation of three-dimensional ice-flow using ascending and descending passes. *IEEE Transactions on Geoscience and Remote Sensing*, 36(1), 25–37. <https://doi.org/10.1109/36.655315>

Kalman, R. E. (1960). A new approach to linear filtering and prediction problems. *Journal of Basic Engineering*, 82(1), 35–45. <https://doi.org/10.1115/1.3662552>

Kang, Y., Lu, Z., Zhao, C., & Qu, W. (2023). Inferring slip-surface geometry and volume of creeping landslides based on InSAR: A case study in Jinsha river basin. *Remote Sensing of Environment*, 294, 113620. <https://doi.org/10.1016/j.rse.2023.113620>

Kankaku, Y., Arikawa, Y., Miura, S., Motohka, T., & Kojima, Y., & Ilee. (2023). ALOS-4 system design and PFM current status. In *Paper Presented at the IEEE International Geoscience and Remote Sensing Symposium (IGARSS)*. IEEE. <https://doi.org/10.1109/IGARSS52108.2023.10283383>

Karanam, V., & Lu, Z. (2023). Hydrocarbon production induced land deformation over Permian Basin; analysis using persistent scatterer interferometry and numerical modeling. *International Journal of Applied Earth Observation and Geoinformation*, 122, 103424. <https://doi.org/10.1016/j.jag.2023.103424>

Kellndorfer, J., Cartus, O., Lavalley, M., Magnard, C., Milillo, P., Oveisgharan, S., et al. (2022). Global seasonal Sentinel-1 interferometric coherence and backscatter data set. *Scientific Data*, 9(1), 73. <https://doi.org/10.1038/s41597-022-01189-6>

Lacroix, P., Handwerger, A. L., & Bièvre, G. (2020). Life and death of slow-moving landslides. *Nature Reviews Earth and Environment*, 1(8), 404–419. <https://doi.org/10.1038/s43017-020-0072-8>

Liu, J., Hu, J., Li, Z., Sun, Q., Ma, Z., Zhu, J., & Wen, Y. (2022). Dynamic estimation of multi-dimensional deformation time series from InSAR based on Kalman filter and strain model. *IEEE Transactions on Geoscience and Remote Sensing*, 60, 1–16. <https://doi.org/10.1109/tgrs.2021.3125574>

Liu, N., Dai, W., Santerre, R., Hu, J., Shi, Q., & Yang, C. (2018). High spatio-temporal resolution deformation time series with the fusion of InSAR and GNSS data using spatio-temporal random effect model. *IEEE Transactions on Geoscience and Remote Sensing*, 57(1), 364–380. <https://doi.org/10.1109/tgrs.2018.2854736>

Liu, X., Zhao, C., Zhang, Q., Lu, Z., & Li, Z. (2020). Deformation of the Baige landslide, Tibet, China, revealed through the integration of cross-platform ALOS/PALSAR-1 and ALOS/PALSAR-2 SAR observations. *Geophysical Research Letters*, 47(3), e2019GL086142. <https://doi.org/10.1029/2019gl086142>

Mehrabi, H. (2021). Three-dimensional strain descriptors at the Earth's surface through 3D retrieved co-event displacement fields of differential interferometric synthetic aperture radar. *Journal of Geodesy*, 95(4), 39. <https://doi.org/10.1007/s00190-021-01489-6>

Michel, R., Avouac, J.-P., & Taboury, J. (1999). Measuring near field coseismic displacements from SAR images: Application to the Landers earthquake. *Geophysical Research Letters*, 26(19), 3017–3020. <https://doi.org/10.1029/1999gl900524>

NISAR. (2018). *NASA-ISRO SAR (NISAR) mission science users' handbook*. Jet Propulsion Laboratory, California Institute of Technology.

Parker, E. (1979). Progress report—Hooskanaden creek slide drilling. *Oregon Coast Highway/Curry County*.

Samsonov, S. (2019). Three-dimensional deformation time series of glacier motion from multiple-aperture DInSAR observation. *Journal of Geodesy*, 93(12), 2651–2660. <https://doi.org/10.1007/s00190-019-01325-y>

- Samsonov, S., Dille, A., Dewitte, O., Kervyn, F., & d'Oreye, N. (2020). Satellite interferometry for mapping surface deformation time series in one, two and three dimensions: A new method illustrated on a slow-moving landslide. *Engineering Geology*, 266, 105471. <https://doi.org/10.1016/j.enggeo.2019.105471>
- Shi, X., Hu, X., Sitar, N., Kayen, R., Qi, S., Jiang, H., et al. (2021). Hydrological control shift from river level to rainfall in the reactivated Guobu slope besides the Laxiwa hydropower station in China. *Remote Sensing of Environment*, 265, 112664. <https://doi.org/10.1016/j.rse.2021.112664>
- Thompson, A. A. (2015). Overview of the RADARSAT constellation mission. *Canadian Journal of Remote Sensing*, 41(5), 401–407. <https://doi.org/10.1080/07038992.2015.1104633>
- Tomás, R., Li, Z., Liu, P., Singleton, A., Hoey, T., & Cheng, X. (2014). Spatiotemporal characteristics of the Huangtupo landslide in the Three Gorges region (China) constrained by radar interferometry. *Geophysical Journal International*, 197(1), 213–232. <https://doi.org/10.1093/gji/ggu017>
- Wang, C., Cai, J., Li, Z., Mao, X., Feng, G., & Wang, Q. (2018). Kinematic parameter inversion of the slumgullion landslide using the time series offset tracking method with UAVSAR data. *Journal of Geophysical Research: Solid Earth*, 123(9), 8110–8124. <https://doi.org/10.1029/2018jb015701>
- Wang, J. L., Deng, Y. K., Wang, R., Ma, P. F., & Lin, H. (2019). A small-baseline InSAR inversion algorithm combining a smoothing constraint and L-1-norm minimization. *IEEE Geoscience and Remote Sensing Letters*, 16(7), 1061–1065. <https://doi.org/10.1109/LGRS.2019.2893422>
- Xiong, Z., Feng, G., Feng, Z., Miao, L., Wang, Y., Yang, D., & Luo, S. (2020). Pre- and post-failure spatial-temporal deformation pattern of the Baige landslide retrieved from multiple radar and optical satellite images. *Engineering Geology*, 279, 105880. <https://doi.org/10.1016/j.enggeo.2020.105880>
- Xu, Y., Lu, Z., Schulz, W. H., & Kim, J. (2020). Twelve-year dynamics and rainfall thresholds for alternating creep and rapid movement of the Hooskanaden landslide from integrating InSAR, pixel offset tracking, and Borehole and hydrological measurements. *Journal of Geophysical Research: Earth Surface*, 125(10), e2020JF005640. <https://doi.org/10.1029/2020jf005640>
- Xu, Y., Schulz, W. H., Lu, Z., Kim, J., & Baxstrom, K. (2021). Geologic controls of slow-moving landslides near the US West Coast. *Landslides*, 18(10), 3353–3365. <https://doi.org/10.1007/s10346-021-01732-3>
- Xu, Y. K., George, D. L., Kim, J., Lu, Z., Riley, M., Griffin, T., & de la Fuente, J. (2021). Landslide monitoring and runoff hazard assessment by integrating multi-source remote sensing and numerical models: An application to the gold basin landslide complex, northern Washington. *Landslides*, 18(3), 1131–1141. <https://doi.org/10.1007/s10346-020-01533-0>
- Yang, Y., Song, L., & Xu, T. (2002). Robust estimator for correlated observations based on bifactor equivalent weights. *Journal of Geodesy*, 76(6–7), 353–358. <https://doi.org/10.1007/s00190-002-0256-7>
- Ye, X., Zhu, H.-H., Chang, F.-N., Xie, T.-C., Tian, F., Zhang, W., & Catani, F. (2024). Revisiting spatiotemporal evolution process and mechanism of a giant reservoir landslide during weather extremes. *Engineering Geology*, 332, 107480. <https://doi.org/10.1016/j.enggeo.2024.107480>
- Ye, X., Zhu, H. H., Wang, J., Zheng, W. J., Zhang, W., Schenato, L., et al. (2024). Towards hydrometeorological thresholds of reservoir-induced landslide from subsurface strain observations. *Science China Technological Sciences*, 67(6), 1907–1922. <https://doi.org/10.1007/s11431-023-2657-3>
- Zhang, H., He, S., Liu, W., Deng, Y., & Hu, W. (2023). Creep-to-Runout transition of large landslides controlled by frictional velocity strengthening and weakening (Vajont 1963, Italy). *Rock Mechanics and Rock Engineering*, 56(11), 1–13. <https://doi.org/10.1007/s00603-023-03473-2>
- Zheng, W. J., Hu, J., Lu, Z., Hu, X., Sun, Q., Liu, J. H., & Li, Z. W. (2023). Enhanced kinematic inversion of 3-D displacements, geometry, and hydraulic properties of a North-South slow-moving landslide in three gorges reservoir. *Journal of Geophysical Research-Solid Earth*, 128(6), 21. <https://doi.org/10.1029/2022jb026232>

References From the Supporting Information

- Kampes, B. M. (2006). *Radar Interferometry: Persistent scatterer technique*. Springer Netherlands.
- Liu, J., Hu, J., Li, Z., Ma, Z., Wu, L., Jiang, W., & Zhu, J. (2022). Complete three-dimensional coseismic displacements due to the 2021 Maduo earthquake in Qinghai Province, China from Sentinel-1 and ALOS-2 SAR images. *Science China Earth Sciences*, 65(4), 687–697. <https://doi.org/10.1007/s11430-021-9868-9>
- Moghtased-Azar, K., & Grafarend, E. W. (2009). Surface deformation analysis of dense GPS networks based on intrinsic geometry: Deterministic and stochastic aspects. *Journal of Geodesy*, 83(5), 431–454. <https://doi.org/10.1007/s00190-008-0252-7>
- Vanicek, P., Grafarend, E. W., & Berber, M. (2008). Short note: Strain invariants. *Journal of Geodesy*, 82(4–5), 263–268. <https://doi.org/10.1007/s00190-007-0175-8>